Superconducting Energy Gap in 1960

Ivar Giaever

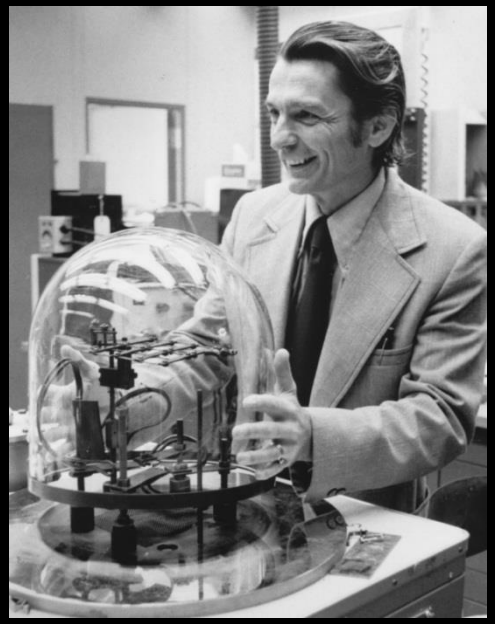

Nobel Prize in 1973

©Schenectady Museum

Tunneling junction

S I N

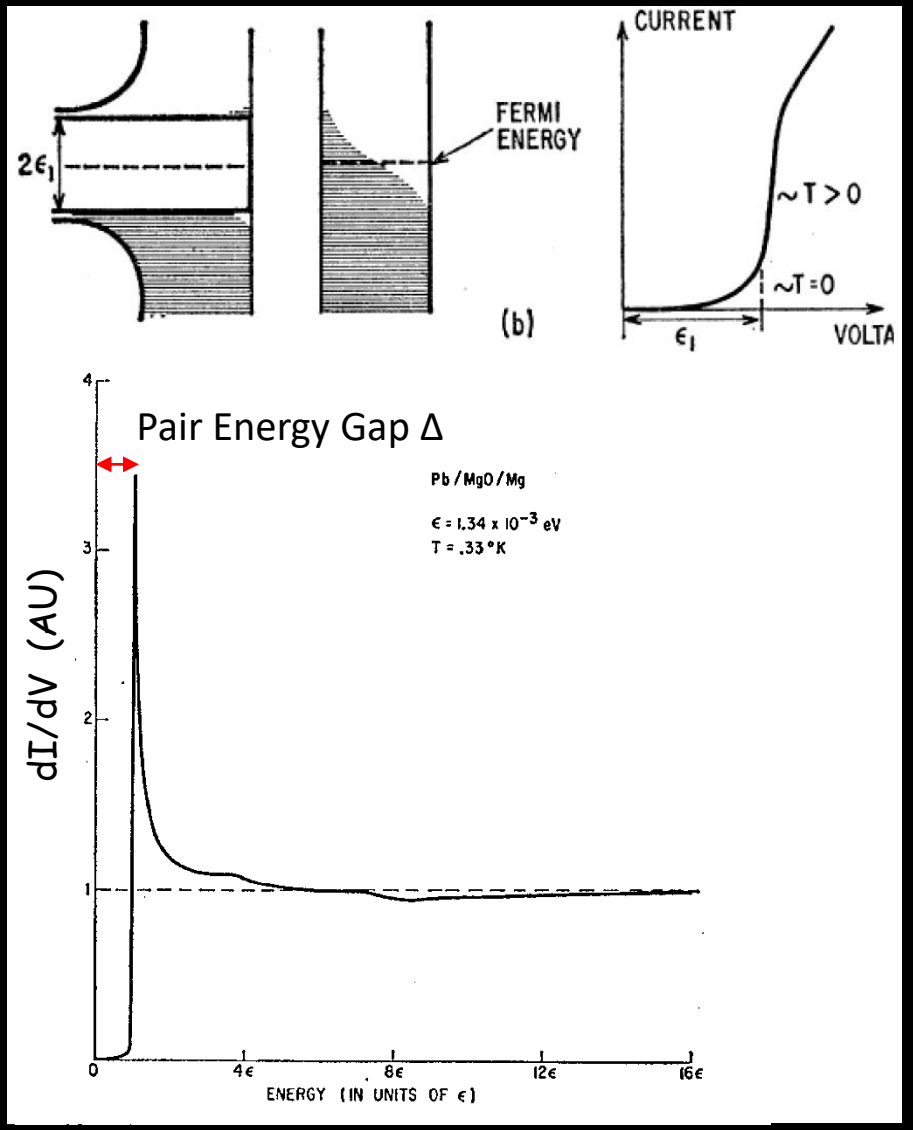

Ivar Giaever, Phys. Rev. Lett. 5, 147 (1960)
I. Giaever, Phys. Rev. 126, 941 (1962)

Single Particle Tunneling

If the barrier is sufficiently thin (less than 10 or 20Å) there is a significant probability that an electron which impinges on the barrier will pass from one metal to the other: this is called tunneling.

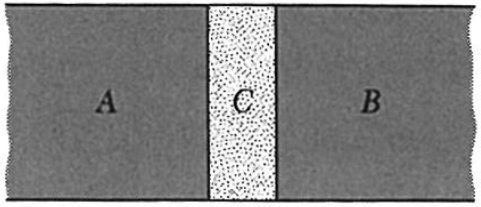

Figure 20 Two metals, *A* and *B*, separated by a thin layer of an insulator *C*.

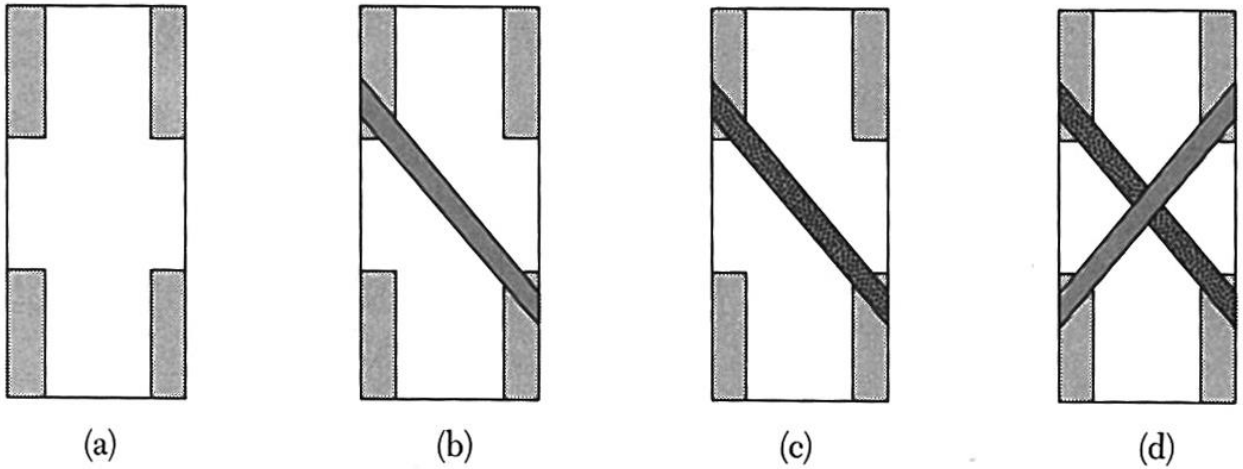

Figure 21 Preparation of an $Al/Al_2O_3/Sn$ sandwich. (a) Glass slide with indium contacts. (b) An aluminum strip 1 mm wide and 1000 to 3000 Å thick has been deposited across the contacts. (c) The aluminum strip has been oxidized to form an Al_2O_3 layer 10 to 20 Å in thickness. (d) A tin film has been deposited across the aluminum film, forming an $Al/Al_2O_3/Sn$ sandwich. The external leads are connected to the indium contacts; two contacts are used for the current measurement and two for the voltage measurement. (After Giaever and Megerle.)

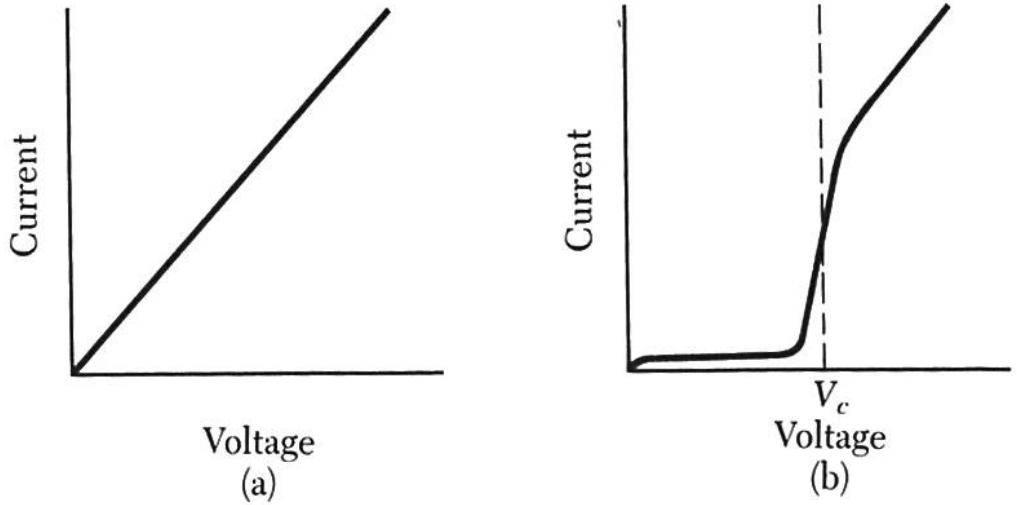

N-N tunneling **S-N tunneling**

Figure 22 (a) Linear current-voltage relation for junction of normal metals separated by oxide layer; (b) current-voltage relation with one metal normal and the other metal superconducting.

1. When both metals are normal conductors, the current-voltage relation of it is Ohmic at low voltages,

2. Giaever (1960) discovered that if one of the metals becomes superconducting, the current-voltage characteristic changes from the straight line of Fig. 22a to the curve shown in Fig. 22b.

Giaever Tunneling

In the superconductor there is an energy gap centered at the Fermi level. At absolute zero no current can flow until the applied voltage is

$$V = E_g/2e = \Delta/e.$$

$N(E) = E/(E^2-\Delta^2)^{1/2}$

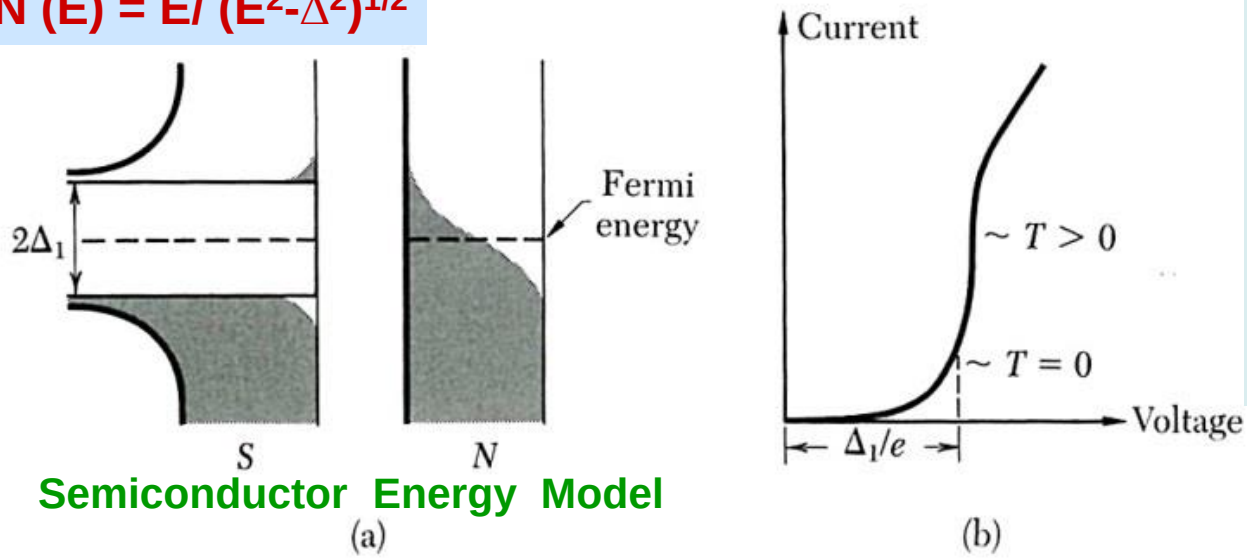

Semiconductor Energy Model

S-N tunneling

At T = 0, **I** is finite when E > Δ,

At T > 0, **I** is > 0 even for E < Δ

Figure 23 The density of orbitals and the current-voltage characteristic for a tunneling junction. In (a) the energy is plotted on the vertical scale and the density of orbitals on the horizontal scale. One metal is in the normal state and one in the superconducting state. (b) I versus V; the dashes indicate the expected break at $T = 0$. (After Giaever and Megerle.)

The current starts when $eV = \Delta$. At finite temperatures, because of electrons in the superconductor that are thermally excited across the energy gap.

Superconducting Tunneling and Application

by L. Solymar

Chapter 4
&
Chapter 5
&
Chapter 6

4.3 Junctions between identical superconductors

The energy diagram for $T = 0°K$ is shown in Fig. 4.4. All energy levels are filled up to $E_F - \Delta$. In thermal equilibrium (Fig. 4.4 (*a*)) there is no current flowing. When a voltage $V < 2\Delta/e$ is applied there is still no current flowing because the electrons below the gap on the left have no access to empty states on the right. At $V = 2\Delta/e$ (Fig. 4.4 (*b*)) there is a sudden rise in current because electrons on the left suddenly gain access to the states above the gap on the right. The corresponding current–voltage characteristic is shown in Fig. 4.4 (*c*).

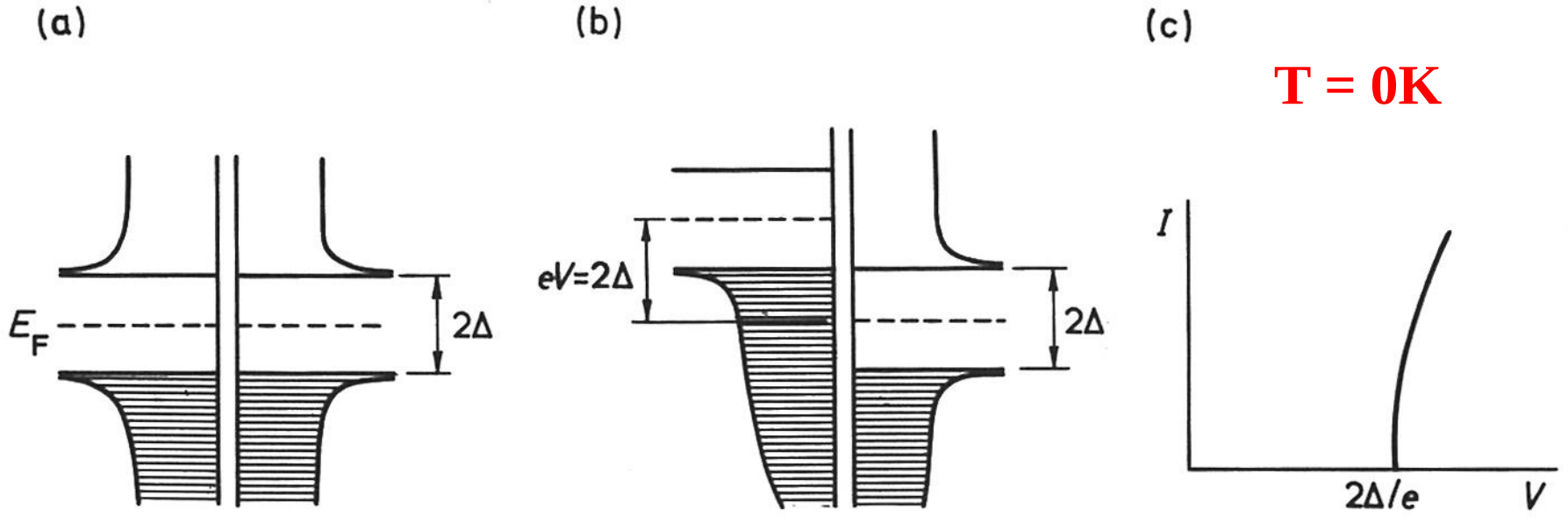

Fig. 4.4 The energy diagram of an SS junction; (*a*) $V = 0$, (*b*) $V = 2\Delta/e$, (*c*) the I–V characteristic at $T = 0$.

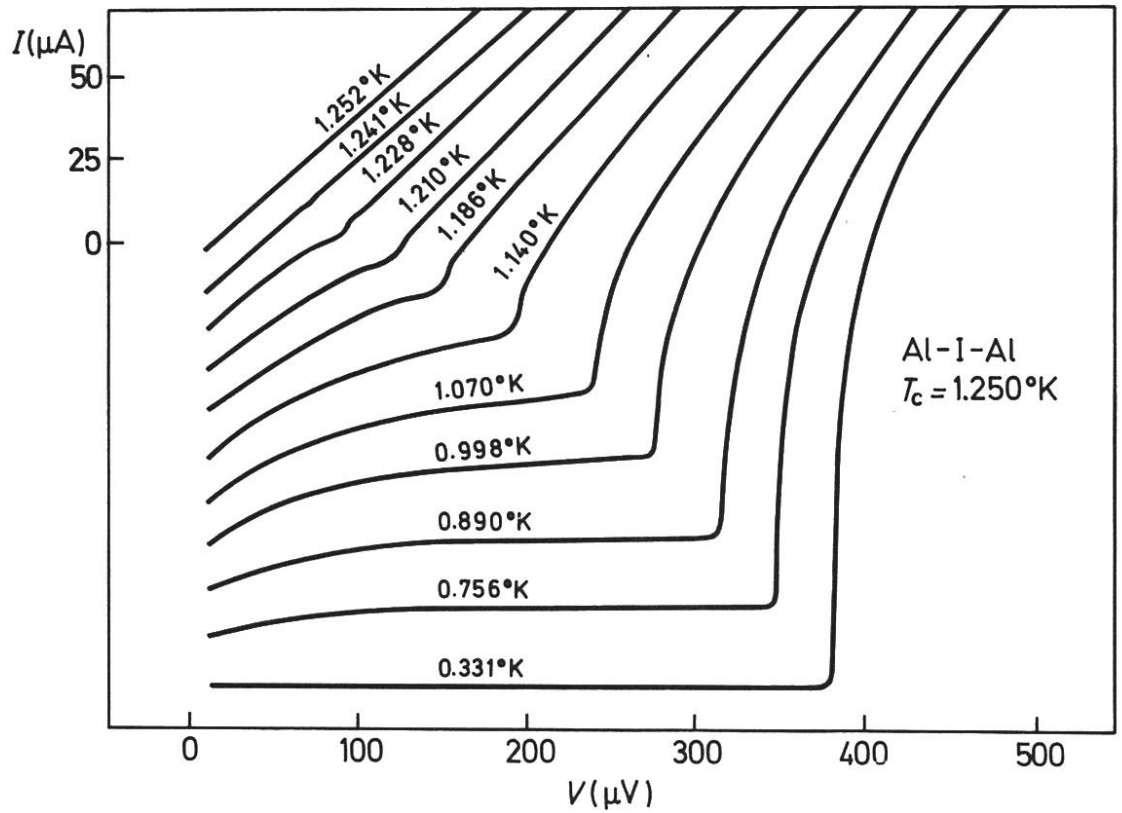

I-V temperature dependence of S/I/S junctions

T_c = 1.250K

For finite temperatures there will be some rounding off* of the sharp features of Fig. 4.4 (*c*) which, of course, depends on the actual temperature (how near it is to the critical). A very neat set of experimental results (Fig. 4.5) by Blackford and March [99] shows the temperature dependence of the current–voltage characteristic for an aluminium–aluminium oxide–aluminium junction. At 1·252°K aluminium is in the normal state and the characteristic is linear. At 1·241°K (a mere 9 millidegrees below the critical temperature) there is already some sign of the energy gap, and it becomes clearly discernible at 1·228°K. As the temperature decreases the knee in the curves moves to higher and higher voltages (corresponding to higher and higher energy gaps). The characteristic at $T = 0{\cdot}331$°K is practically identical to that at 0°K.

4.4 Junctions between superconductors of different energy gap

In the same way as the previously discussed case of identical superconductors, at $T = 0°K$ no current flows until the applied voltage is sufficiently large to bring the bottom of the gap on the left in line with the top of the gap on the right. This occurs at an applied voltage of $V = (\Delta_1 + \Delta_2)/e$ as shown in Fig. 4.6 (*a*). The current–voltage characteristic (Fig. 4.6 (*b*)) is similar to that shown in Fig. 4.4 (*c*) with the sole difference that the current starts rising at a voltage corresponding to the arithmetical mean of the gap energies.

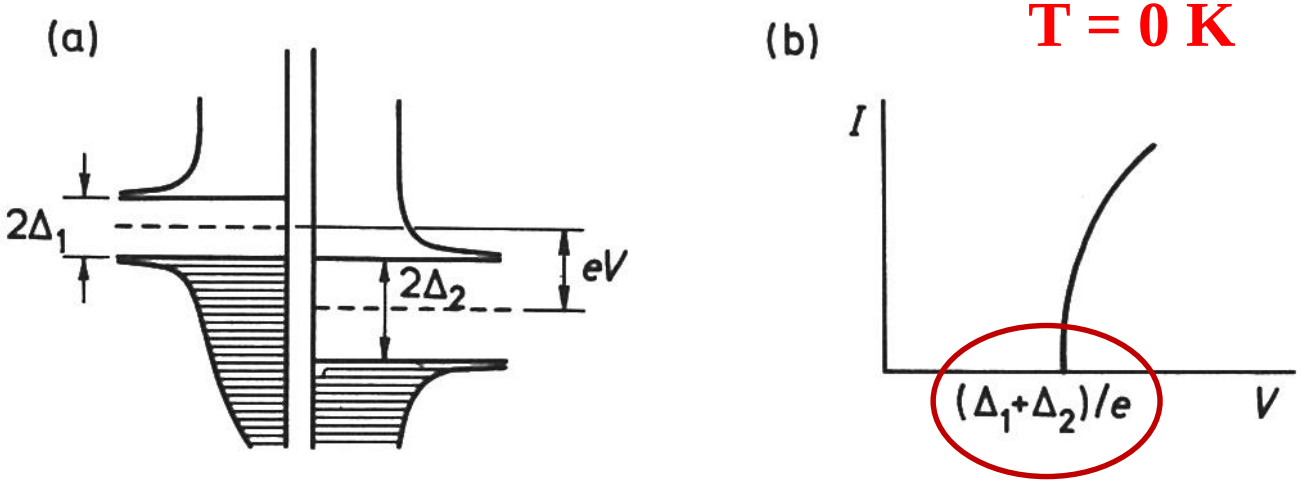

Fig. 4.6 Energy diagram and *I*–*V* characteristic of an S_1S_2 junction at $T = 0$.

T > 0K

At finite temperatures we may still assume that the normal electron states above the larger gap are empty but there are some thermally excited normal electrons in the smaller-gap superconductor as shown in Fig. 4.7 (*a*) for the case of thermal equilibrium.

Applying a voltage the current will start to flow immediately and will increase with increasing voltage (Fig. 4.7 (*e*)) until $V = (\Delta_2 - \Delta_1)/e$. The energy diagram for this case is shown in Fig. 4.7 (*b*); at this stage all electrons above the gap on the left can tunnel across into empty states on the right. What happens when the voltage is increased further? The number of electrons capable to tunnel across is still the same but they face a smaller density of states, as shown in Fig. 4.7 (*c*), hence the current decreases. The decrease in current continues until $V = (\Delta_1 + \Delta_2)/e$. At this point (Fig. 4.7 (*d*)) electrons from below the gap on the left gain access to empty states on the right, and there is a sudden increase in current. Thus the current–voltage characteristic of Fig. 4.7 (*e*) exhibits a negative resistance in the region

$$\frac{\Delta_2 - \Delta_1}{e} < V < \frac{\Delta_2 + \Delta_1}{e} \tag{3.1}$$

S_1/ I /S_2 T > 0K

$\Delta_1 < \Delta_2$

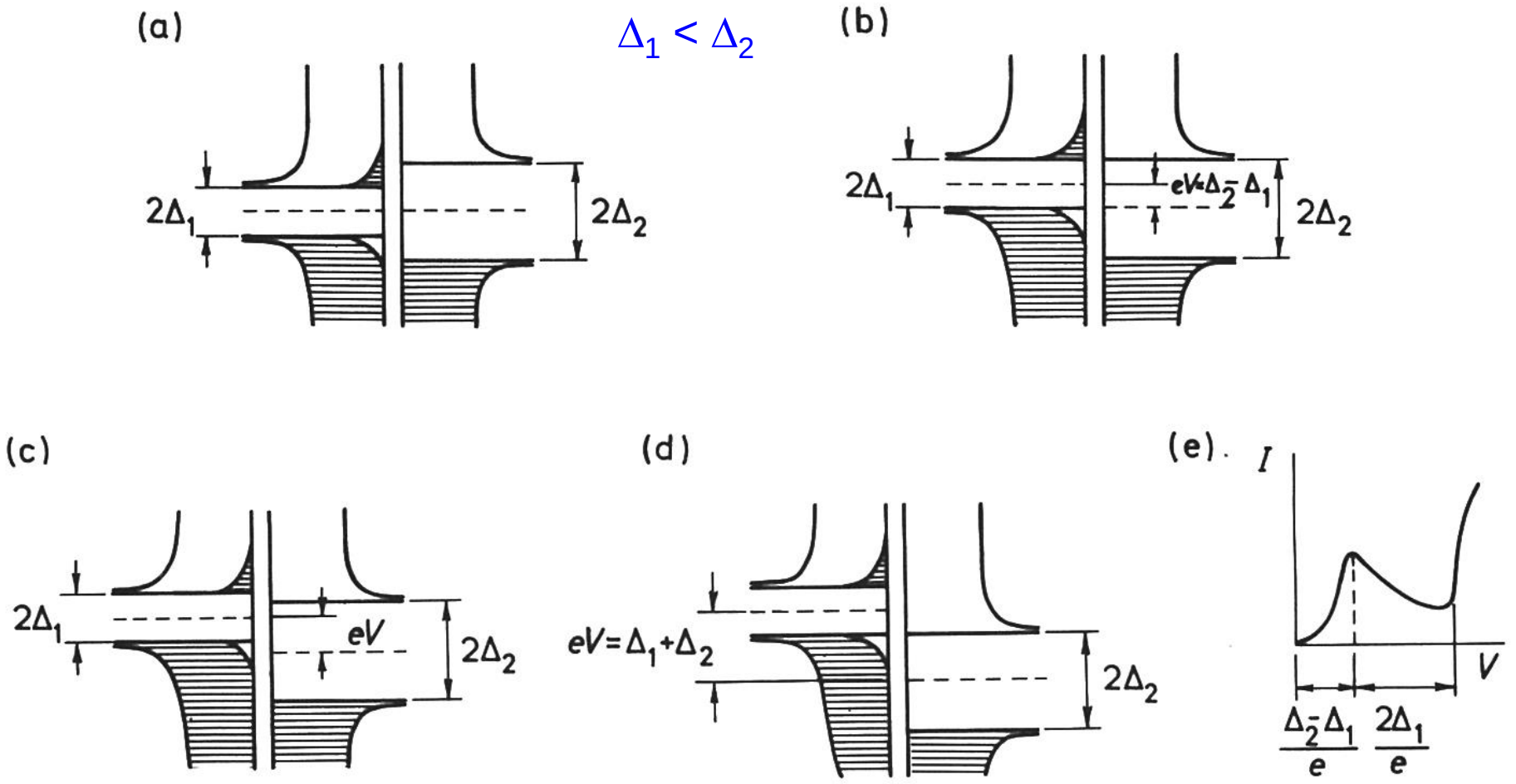

Fig. 4.7 The energy diagram and I–V characteristic of an S_1S_2 junction at finite temperature; (*a*) $V = 0$, (*b*) $V = (\Delta_2 - \Delta_1)/c$, (*c*) $(\Delta_2 - \Delta_1)/e < V < (\Delta_2 + \Delta_1)/e$, (*d*) $V = (\Delta_1 + \Delta_2)/e$, (*e*) the I–V characteristic.

The appearance of a negative resistance was reported simultaneously by Nicol *et al.* [46] and Giaever [45]. A very convincing characteristic presented by the latter author for an Al–Al_2O_3–Pb junction is shown in Fig. 4.8.

The experimentally found dependence [100] of the negative resistance on temperature is shown in Fig. 4.9 for a Sn–SnO–Pb junction. The current–voltage characteristic turns nonlinear when lead becomes superconducting and the negative resistance appears as soon as tin becomes superconducting as well. The negative resistance may be clearly seen down to 2·39°K but not at 1·16°K. Experimentally the negative resistance always disappears at sufficiently low temperatures but that may be due to insufficient accuracy of measurement and to nonideal circumstances.

The presence of a maximum and minimum in the characteristic gives further help in diagnostic measurements aimed at determining the width of the energy gaps. In addition, the negative resistance may be used in devices which will be discussed in more detail in Section 7.1.

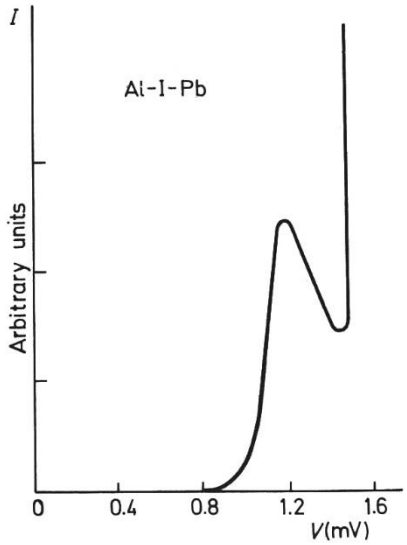

Fig. 4.8 The *I–V* characteristic of an Al–I–Pb junction, both Al and Pb superconducting. After Giaever [45].

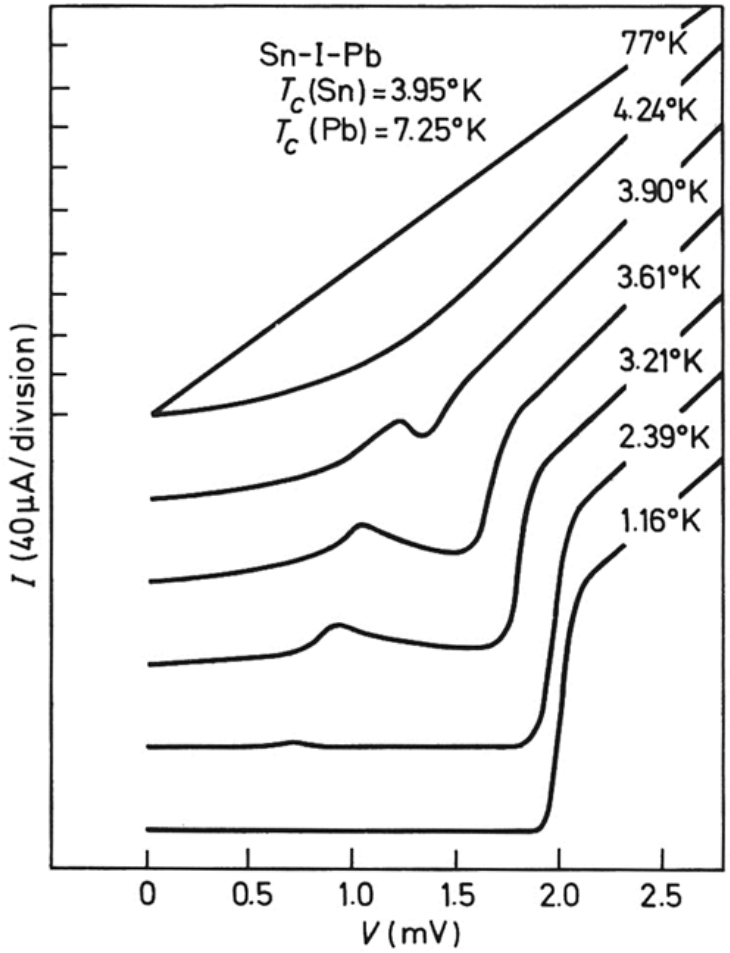

Fig. 4.9 *I–V* characteristics of an Sn–I–Pb junction.

Point contact junctions. These were developed by Levinstein and Kunzler [122, 123] in the form shown in Fig. 4.21. The barrier is prepared by heavily anodising a freshly etched tip of Al, Nb, Ta, etc. The diameter of the junction at the point of contact was estimated to be less than 10 μm. Tunnelling characteristics were observed in a large resistance range from 10^2 to 10^5 ohm.

The advantage of point contacts is that tunnelling measurements can be made on materials not accessible in thin film form. Furthermore, the tunnelling is generally from one single crystal to another since the grain size of the material both in the tip of the point contact and in the bulk is considerably larger than the contact area. Notable success of the point contact technique was to obtain the correct value for the energy gap of Nb_3Sn where thin film measurements consistently gave the wrong value.

was mostly on bulk samples

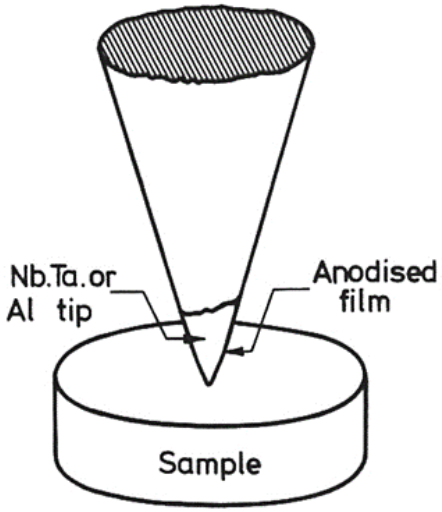

Lead to the invention of STM in 1982 !

Fig. 4.21 Point contact junction. After Levinstein and Kunzler [122].

Josephson Superconductor Tunneling

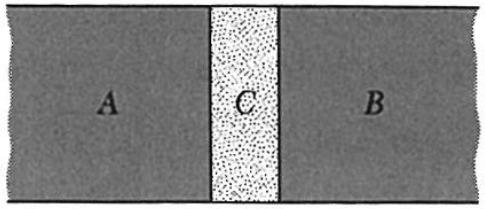

S-I-S
S-N-S

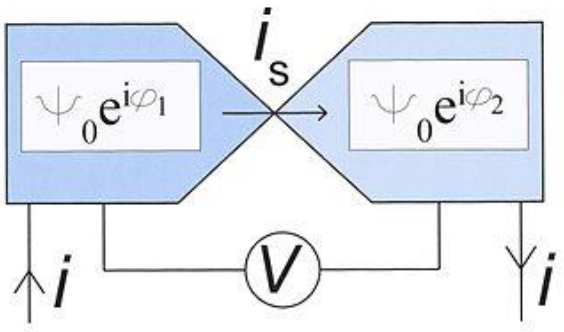

Such a junction is called a weak link.

1. **DC Josephson effect**: A ***dc*** current flows across the junction in the absence of any electric or magnetic field.
2. **AC Josephson effect**: A ***dc*** voltage applied across the junction causes ***rf*** current oscillations across the junction.

   An ***rf*** voltage applied with the ***dc*** voltage can then cause a ***dc*** current across the junction.
3. **Macroscopic long-range quantum interference**: A ***dc*** magnetic field applied through a superconducting circuit containing two junctions causes the maximum supercurrent to show interference effects as a function of magnetic field intensity. SQUID

DC Josephson Effect

Our discussion of Josephson junction phenomena follows the discussion of flux quantization, let both superconductors be identical.

$$i\hbar\frac{\partial\psi_1}{\partial t} = \hbar T\psi_2 \ ; \qquad i\hbar\frac{\partial\psi_2}{\partial t} = \hbar T\psi_1 \ . \tag{38}$$

Here $\hbar T$ represents the effect of the electron-pair coupling or transfer interaction across the insulator; T has the dimensions of a rate or frequency. It is a measure of the leakage of ψ_1 into the region 2, and of ψ_2 into the region 1.

Let $\psi_1 = n_1^{1/2}\, e^{i\theta_1}$ and $\psi_2 = n_2^{1/2}\, e^{i\theta_2}$. Then

$$\frac{\partial\psi_1}{\partial t} = \tfrac{1}{2}n_1^{-1/2}\, e^{i\theta_1}\frac{\partial n_1}{\partial t} + i\psi_1\frac{\partial\theta_1}{\partial t} = -iT\psi_2 \ ; \tag{39}$$

$$\frac{\partial\psi_2}{\partial t} = \tfrac{1}{2}n_2^{-1/2}\, e^{i\theta_2}\frac{\partial n_2}{\partial t} + i\psi_2\frac{\partial\theta_2}{\partial t} = -iT\psi_1 \ . \tag{40}$$

We multiply (39) by $n_1^{1/2}\, e^{-i\theta_1}$ to obtain, with $\delta \equiv \theta_2 - \theta_1$,

$$\frac{1}{2}\frac{\partial n_1}{\partial t} + in_1\frac{\partial\theta_1}{\partial t} = -iT(n_1n_2)^{1/2}\, e^{i\delta} \ . \tag{41}$$

We multiply (40) by $n_2^{1/2}\, e^{-i\theta_2}$ to obtain

$$\frac{1}{2}\frac{\partial n_2}{\partial t} + in_2\frac{\partial\theta_2}{\partial t} = -iT(n_1n_2)^{1/2}\, e^{-i\delta} \ . \tag{42}$$

Now equate the real and imaginary parts of (41) and similarly of (42):

eq (41); eq(42)

For the real part

$$\frac{\partial n_1}{\partial t} = 2T(n_1 n_2)^{1/2} \sin \delta \; ; \qquad \frac{\partial n_2}{\partial t} = -2T(n_1 n_2)^{1/2} \sin \delta \; ; \tag{43}$$

For the imaginary part

$$\frac{\partial \theta_1}{\partial t} = -T\left(\frac{n_2}{n_1}\right)^{1/2} \cos \delta \; ; \qquad \frac{\partial \theta_2}{\partial t} = -T\left(\frac{n_1}{n_2}\right)^{1/2} \cos \delta \; . \tag{44}$$

If $n_1 \cong n_2$ as for identical superconductors 1 and 2, we have from (44) that

$$\frac{\partial \theta_1}{\partial t} = \frac{\partial \theta_2}{\partial t} \; ; \qquad \boxed{\frac{\partial}{\partial t}(\theta_2 - \theta_1) = 0} \; . \tag{45}$$

The phase difference is time independent !

$$\frac{\partial n_2}{\partial t} = -\frac{\partial n_1}{\partial t} \; . \tag{46}$$

the current J of superconductor pairs across the junction depends on the phase difference δ as

$$\boxed{J = J_0 \sin \delta = J_0 \sin (\theta_2 - \theta_1) \; ,} \tag{47}$$

J ∝ dN/dt

where J_0 is proportional to the transfer interaction T. The current J_0 is the maximum zero-voltage current that can be passed by the junction. With no applied voltage a dc current will flow across the junction (Fig. 24), with a value between J_0 and $-J_0$ according to the value of the phase difference $\theta_2 - \theta_1$. This is the **dc Josephson effect**.

Josephson Current

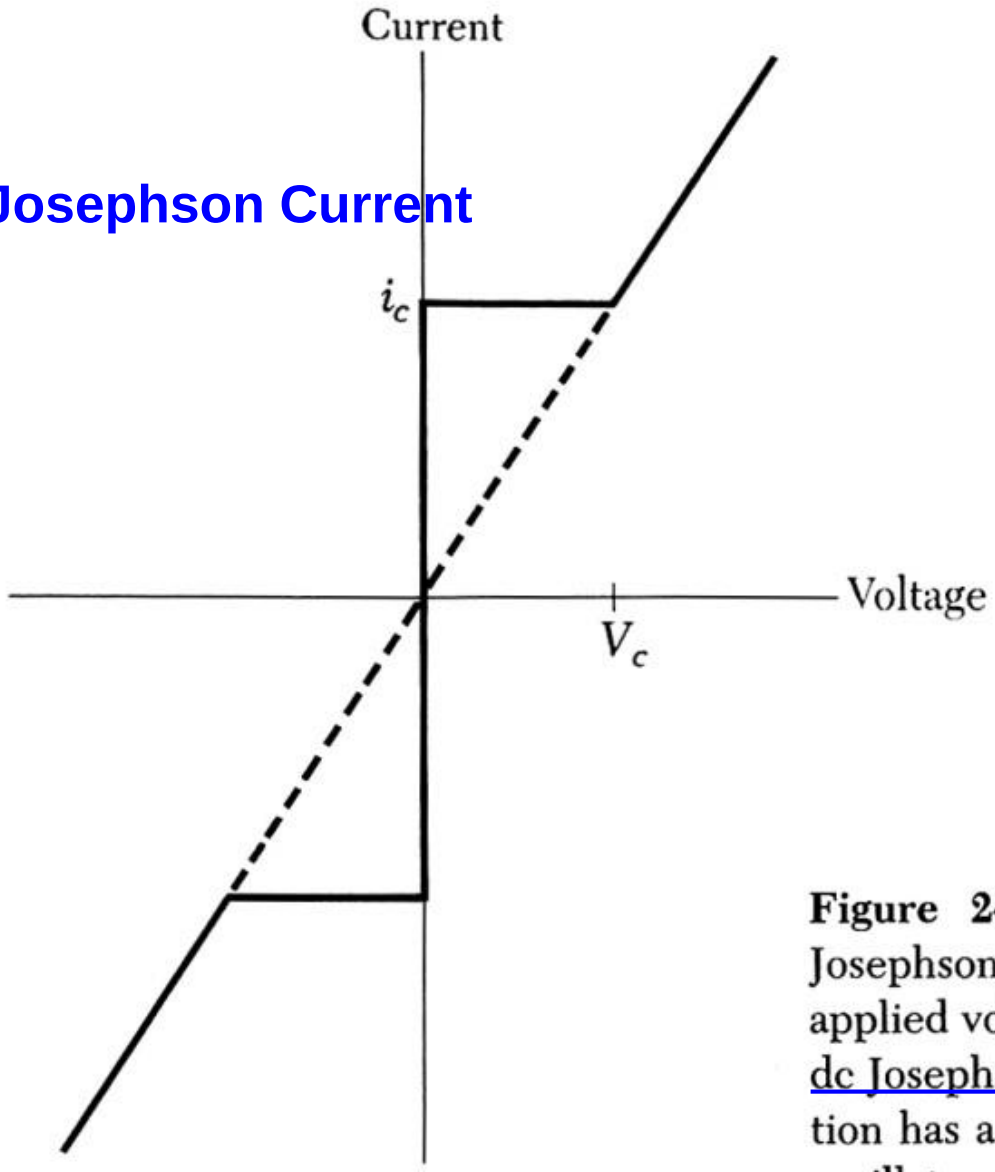

Figure 24 Current-voltage characteristic of a Josephson junction. Dc currents flow under zero applied voltage up to a critical current i_c: this is the dc Josephson effect. At voltages above V_c the junction has a finite resistance, but the current has an oscillatory component of frequency $\omega = 2eV/\hbar$: this is the ac Josephson effect.

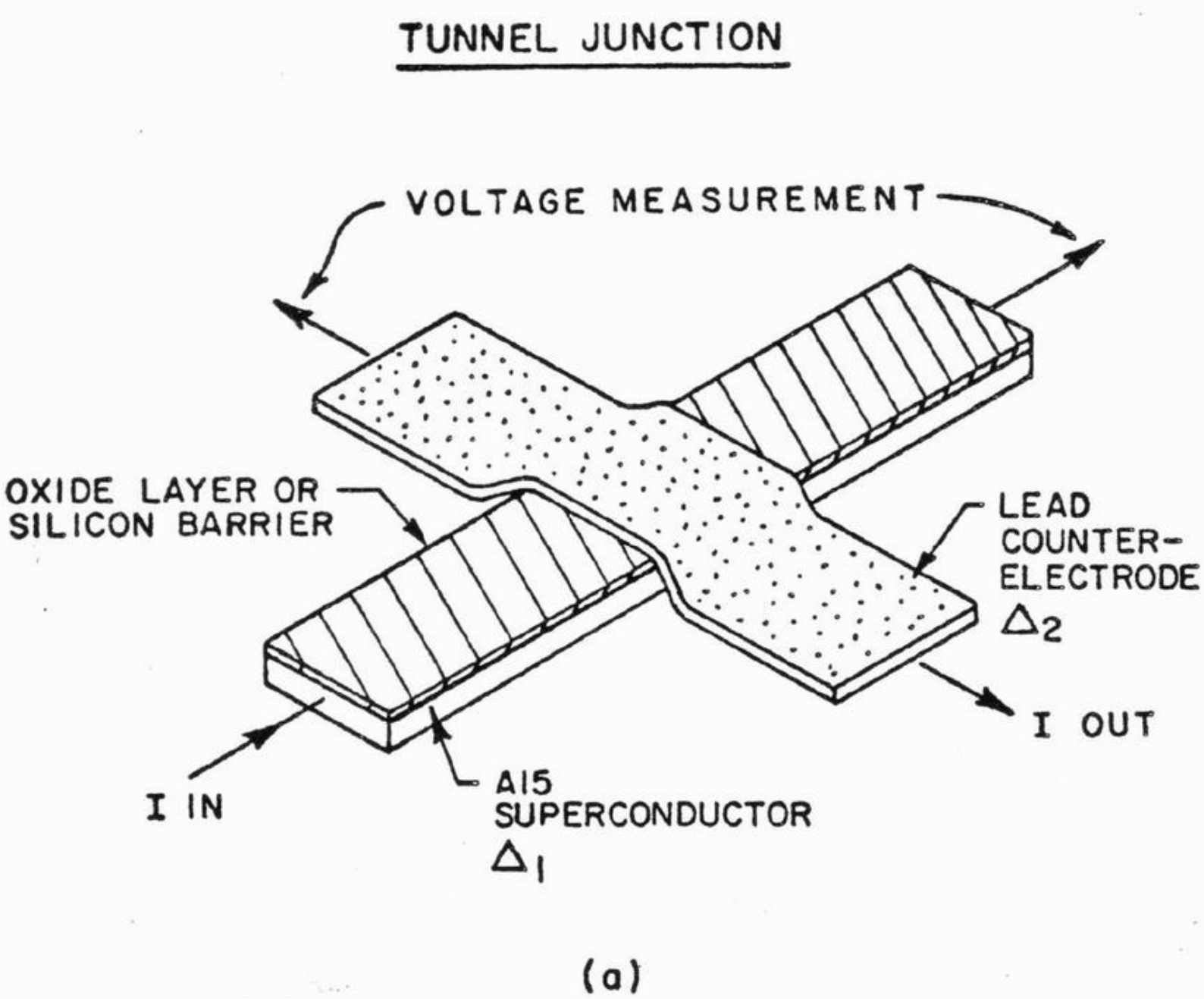

FIG. 1.1--(a) The geometry of our oxide layer tunnel junctions.

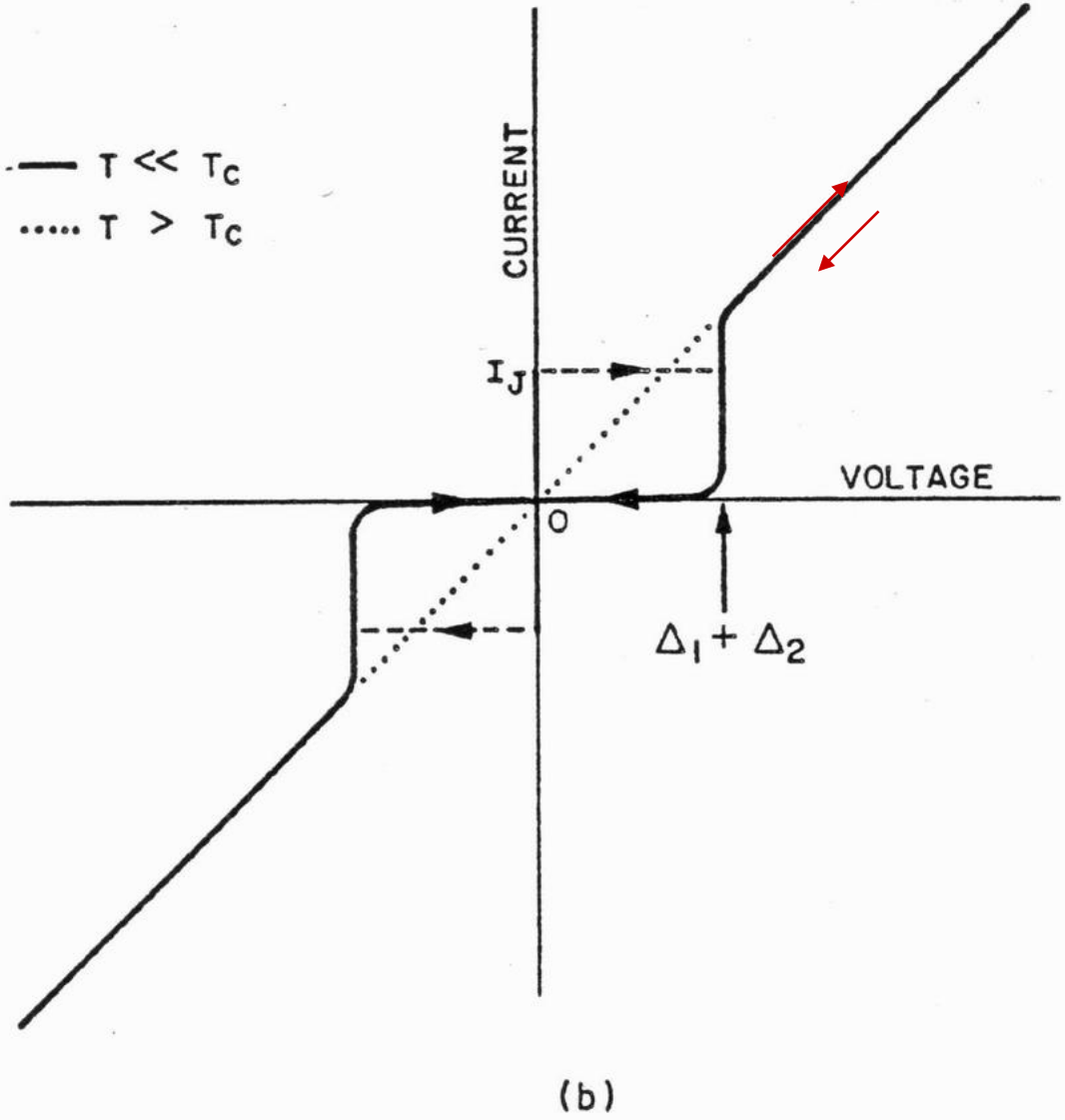

(b)

A two-terminal device !

(b) An idealized current-voltage characteristic showing quasiparticle (Giaever) and pair (Josephson) tunneling through the barrier.

AC Josephson Effect

Under a dc voltage V

We can say that a pair on one side is at potential energy $-eV$ and a pair on the other side is at eV.

$$i\hbar\,\partial\psi_1/\partial t = \hbar T\psi_2 - eV\psi_1; \qquad i\hbar\,\partial\psi_2/\partial t = \hbar T\psi_1 + eV\psi_2 \ . \tag{48}$$

Follow Eq. 41

$$\frac{1}{2}\frac{\partial n_1}{\partial t} + in_1\frac{\partial\theta_1}{\partial t} = ieVn_1\hbar^{-1} - iT(n_1n_2)^{1/2}\,e^{i\delta} \ . \tag{49}$$

This equation breaks up into the real part

$$\partial n_1/\partial t = 2T(n_1n_2)^{1/2}\sin\delta \ , \tag{50}$$

exactly as without the voltage V, and the imaginary part

$$\partial\theta_1/\partial t = (eV/\hbar) - T(n_2/n_1)^{1/2}\cos\delta \ , \tag{51}$$

which differs from (44) by the term $eV/\hbar$.

Follow Eq. 42

$$\frac{1}{2}\frac{\partial n_2}{\partial t} + in_2\frac{\partial\theta_2}{\partial t} = -i\,eVn_2\hbar^{-1} - iT(n_1n_2)^{1/2}\,e^{-i\delta} \ , \tag{52}$$

$$\partial n_2/\partial t = -2T(n_1 n_2)^{1/2} \sin \delta \ ; \tag{53}$$

$$\partial \theta_2/\partial t = -(eV/\hbar) - T(n_1/n_2)^{1/2} \cos \delta \ . \tag{54}$$

with $n_1 \cong n_2$,

$$\partial(\theta_2 - \theta_1)/\partial t = \partial\delta/\partial t = -2eV/\hbar \ . \tag{55}$$

relative phase of the probability amplitudes vary as

$$\delta(t) = \delta(0) - (2eVt/\hbar) \ . \tag{56}$$

$$J = J_0 \sin [\delta(0) - (2eVt/\hbar)] \ . \tag{57}$$

The phase is dependent on time.

The current oscillates with frequency

$$\omega = 2eV/\hbar \ . \tag{58}$$

This is the **ac Josephson effect**. A dc voltage of 1 μV produces a frequency of 483.6 MHz. The relation (58) says that a photon of energy $\hbar\omega = 2eV$ is emitted or absorbed when an electron pair crosses the barrier.

To be used for a precise measurement of $\hbar/e$

Macroscopic Quantum Interference.

We consider two Josephson junctions in parallel, as in Fig. 25.

$\hbar c \nabla\theta = qA$

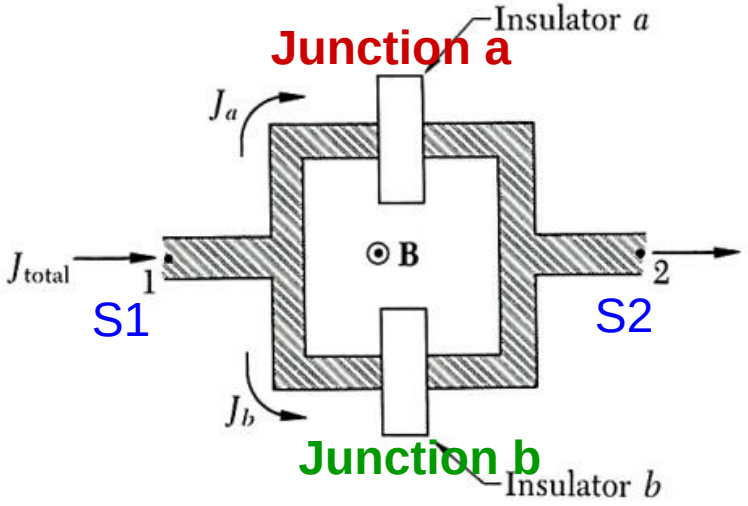

$\theta_1 - \theta_2 = (2e/\hbar c)\Phi$ eq. (59)

Figure 25 The arrangement for experiment on macroscopic quantum interference. A magnetic flux Φ passes through the interior of the loop.

Now let the flux Φ pass through the interior of the circuit.
By (59), $\delta_b - \delta_a = (2e/\hbar c)\Phi$, or

$$\delta_b = \delta_0 + \frac{e}{\hbar c}\Phi \ ; \qquad \delta_a = \delta_0 - \frac{e}{\hbar c}\Phi \ . \tag{60}$$

The total current is the sum of J_a and J_b.

$$J_{\text{Total}} = J_a + J_b = J_0\left\{\sin\left(\delta_0 + \frac{e}{\hbar c}\Phi\right) + \sin\left(\delta_0 - \frac{e}{\hbar c}\Phi\right)\right\} = 2(J_0 \sin\delta_0)\cos\frac{e\Phi}{\hbar c} .$$

The current varies with Φ and has maxima when

$$e\Phi/\hbar c = s\pi \ , \qquad s = \text{integer} \ . \tag{61}$$

Double slit diffraction pattern for two tunnel junctions

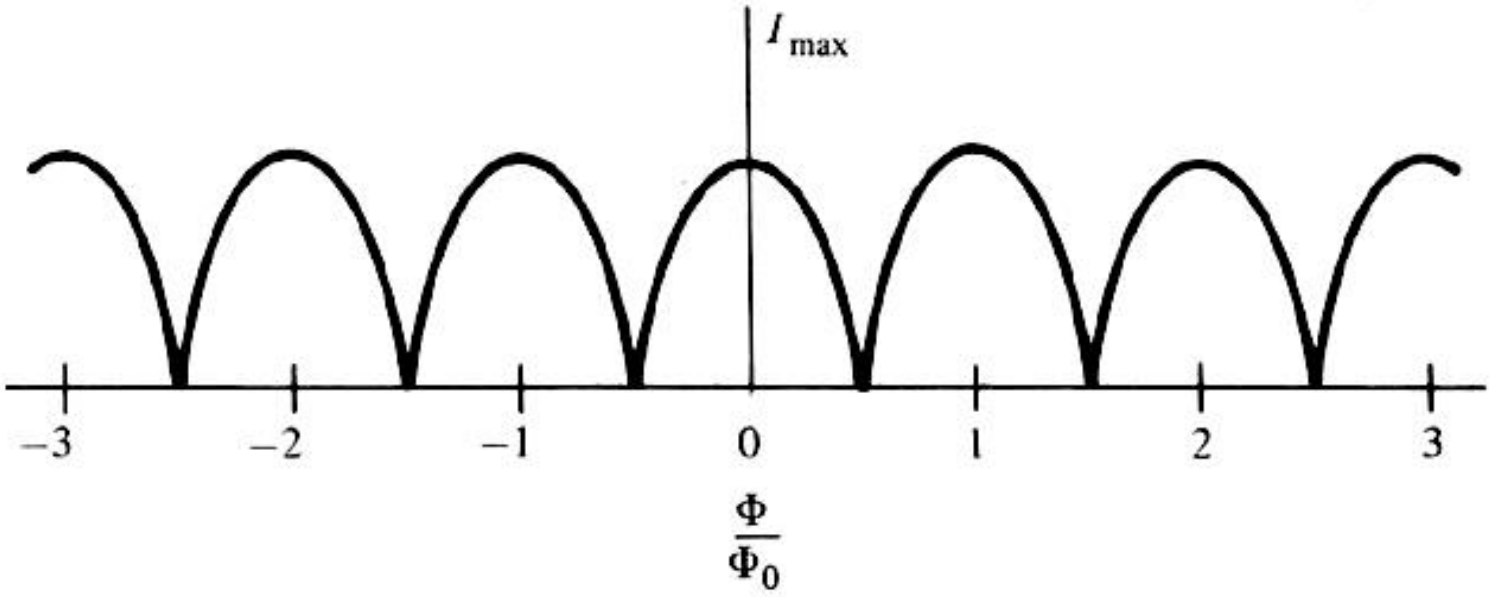

FIGURE 6-5
Dependence of maximum supercurrent through symmetrical two-junction superconducting interferometer (SQUID), shown schematically in Fig. 6-4.

Tinkham, Chapter 6, p. 203.

Single slit diffraction for single tunnel junction

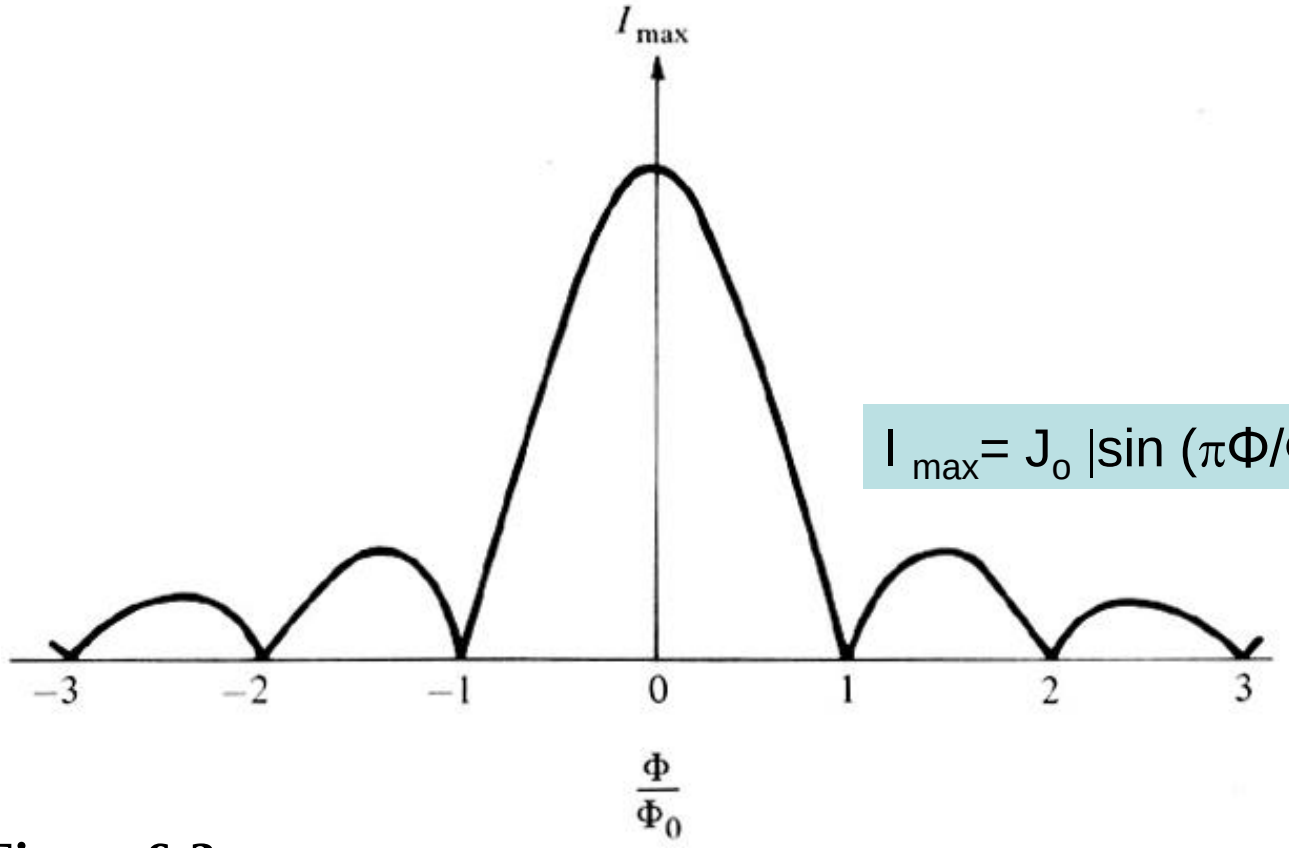

$I_{max} = J_o |\sin(\pi\Phi/\Phi_o)/\pi\Phi/\Phi_o|$

Figure 6-3

Dependence of maximum supercurrent through a **single Josephson junction** upon the flux threading the junction. The resemblance to the "single-slit" diffraction pattern of optics is evident.

Tinkham, Chapter 6, p. 199

The periodicity of the current is shown in Fig. 26.

1. The **short period** variation is produced by interference from the two junctions, as predicted by (61).
2. The **longer period** variation is a diffraction effect and arises from the finite dimensions of each junction.

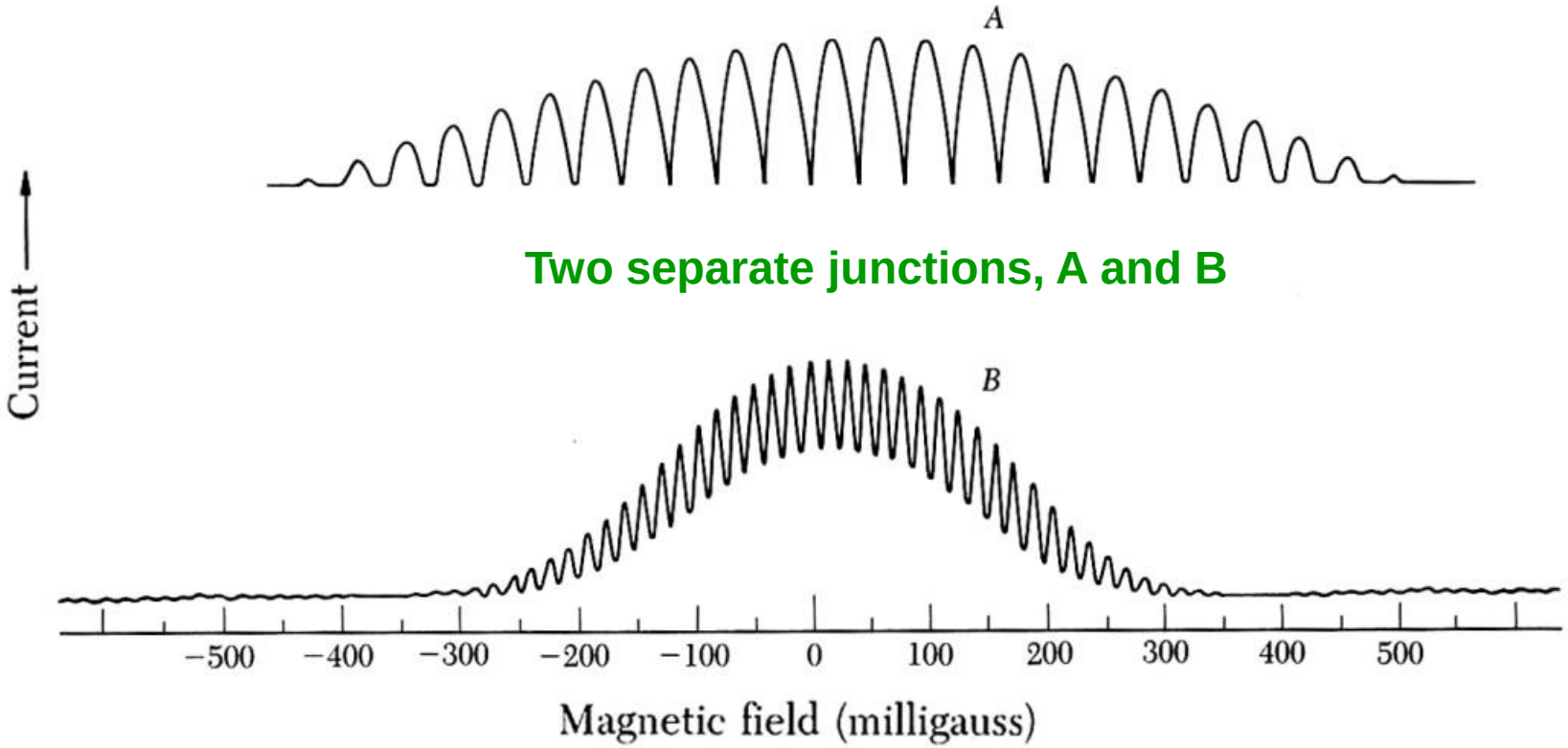

Figure 26 Experimental trace of J_{max} versus magnetic field showing interference and diffraction effects for two junctions A and B. The field periodicity is 39.5 and 16 mG for A and B, respectively. Approximate maximum currents are 1 mA (A) and 0.5 mA (B). The junction separation is 3 mm and junction width 0.5 mm for both cases. The zero offset of A is due to a background magnetic field. (After R. C. Jaklevic, J. Lambe, J. E. Mercereau and A. H. Silver.)

5.2 Photon-assisted tunnelling

Read the Book of Solymar

The tunnelling current may be modified by illuminating the junction with electromagnetic waves. It is easy to see that if the energy of the incident photons is in excess of 2Δ they will break up Cooper-pairs and create two electrons above the gap as shown in Fig. 5.5 (*a*). Since the number of electrons above the gap increases this way above its equilibrium value, some of these extra electrons will tunnel across the barrier (Fig. 5.5 (*b*)) creating thereby an extra current. We shall return to this problem in Section 7.2, for the moment we shall concentrate on the case when the energy of the incident photon is insufficient to break up a Cooper-pair. Influence on the tunnelling characteristics is still possible then if the photons act jointly with the applied voltage.

T = 0K

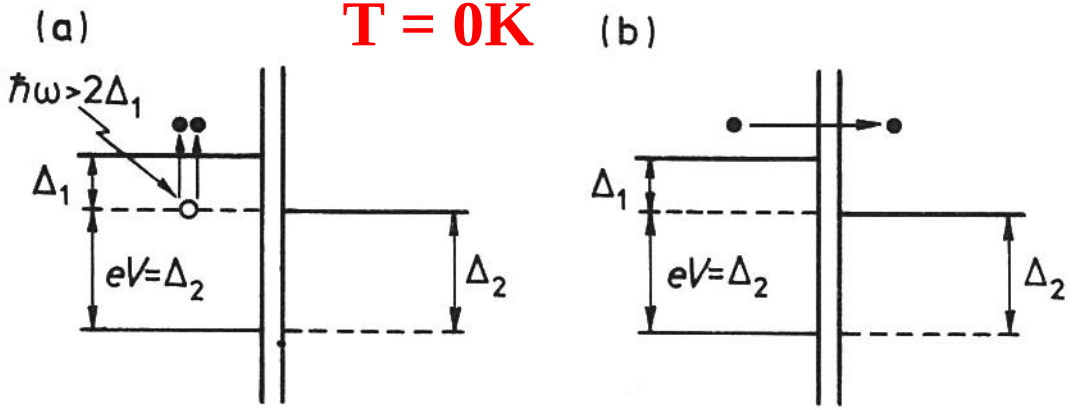

Fig. 5.5 Effect of incident photons on a tunnel junction; (*a*) a photon creates two electrons by breaking up a Cooper-pair, (*b*) one of the electrons created tunnels across.

Let us take $T = 0°K$ again and recall the case when $V = (\Delta_1 + \Delta_2)/e$. Then a Cooper-pair may break up into two electrons, one of them tunnelling across the barrier as has been shown in Fig. 4.12. If $V < (\Delta_1 + \Delta_2)/e$ no current flows. A Cooper-pair breaking up could not cause a current because the transition shown in Fig. 5.6 (*a*) with dotted lines is not permissible. However, if a photon of the right energy is available the liberated electron may follow the path shown in Fig. 5.6 (*b*) and get into an allowed state just above the gap. We may say that the electron tunnelled across the barrier by absorbing a photon, and refer to the phenomenon as photon-assisted tunnelling. The mathematical condition for the onset of tunnelling current is

$$\hbar\omega = \Delta_1 + \Delta_2 - eV. \qquad (5.1)$$

T = 0K

for $eV < \Delta_1 + \Delta_2$

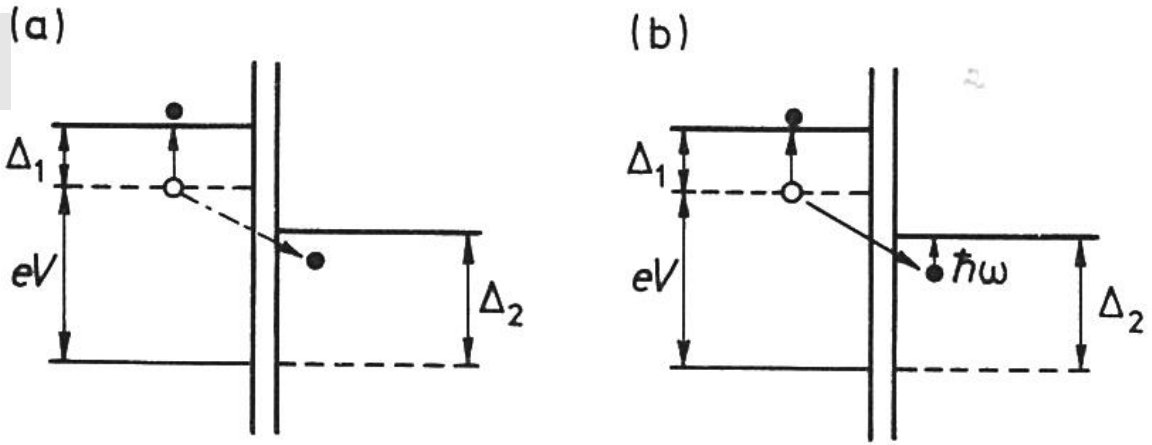

Fig. 5.6 (*a*) Tunnelling not allowed. (*b*) Tunnelling allowed if assisted by a photon.

If the energy of the photon is above this value tunnelling is still possible, though with a reduced probability because of a less favourable density of states. If the energy of the incident photon is below the value given by Equation (5.1) tunnelling may still be possible with the aid of a multi-photon process. An electron absorbing for example three photons simultaneously may tunnel across the barrier in the way shown in Fig. 5.7 (*a*). Hence we may expect sudden rises in the tunnelling characteristics whenever the condition

T = 0K

$$n\hbar\omega = \Delta_1 + \Delta_2 - eV \qquad (5.2)$$

is satisfied, that is for a series of voltages in the range $0 < V < (\Delta_1 + \Delta_2)/e$.

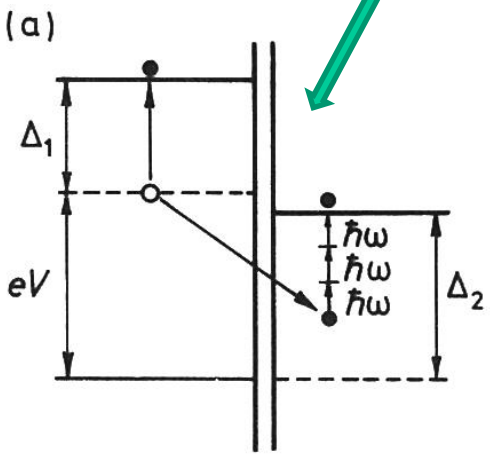

$eV - \Delta_1 + n\hbar\omega = \Delta_2$

$n\hbar\omega = \Delta_1 + \Delta_2 - eV$

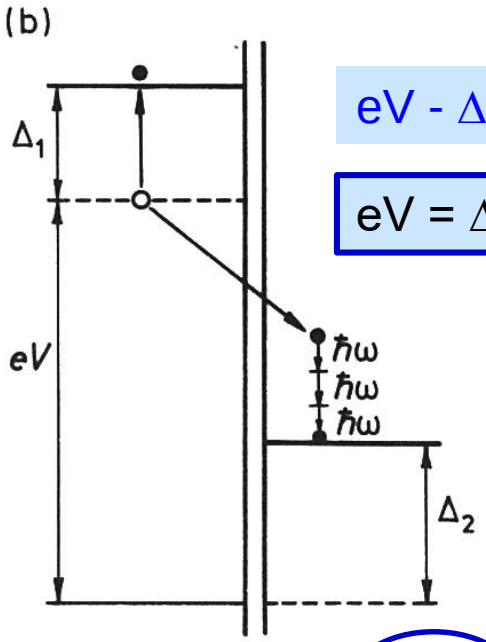

$eV - \Delta_1 - n\hbar\omega = \Delta_2$

$eV = \Delta_1 + \Delta_2 + n\hbar\omega$

Fig. 5.7 Tunnelling assisted (*a*) by absorption of three photons, (*b*) by emission of three photons.

For $eV > \Delta_1 + \Delta_2$

When $V > (\Delta_1 + \Delta_2)/e$ we know that a tunnelling current will flow even in the absence of an incident electromagnetic wave. However, if photons of the right energy are available they can assist the tunnelling in this case as well, as shown in Fig. 5.7 (*b*) for a three-photon process. A Cooper-pair breaks up; one of the electrons goes into a state just above the gap on the left, and the other electron tunnels across into the superconductor on the right at an energy demanded by energy conservation (the sum of electron energies must equal the energy of the Cooper-pair). This process would occur with much higher probability if the electron could tunnel into the high density states lying just above the gap on the right. In Fig. 5.7 (*b*) this becomes energetically possible when three photons are *emitted* at the same time. Thus the mechanism of current rise is photon emission *stimulated* by input photons. For an *n*-photon emission process the current rises occur when

T = 0K

$$V_n = \frac{1}{e}(\Delta_1 + \Delta_2 + n\hbar\omega). \qquad (5.3)$$

T > 0K

For finite temperatures there is one more instance where electrons tunnel between maximum density states and that occurs at $V = (\Delta_2 - \Delta_1)/e$, as shown in Fig. 5.8 (*a*). Tunnelling between those states may also be assisted by photons as shown in Figs. 5.8 (*b* and *c*) for photon absorption and emission respectively. In general, multi-photon absorptions and emissions are possible again, and thus for finite temperatures there is another set of voltages,

$$V_m = \frac{1}{e}(\Delta_2 - \Delta_1 + m\hbar\omega), \qquad m = \pm 1, \pm 2, \pm 3 \tag{5.4}$$

at which current rises can be expected.

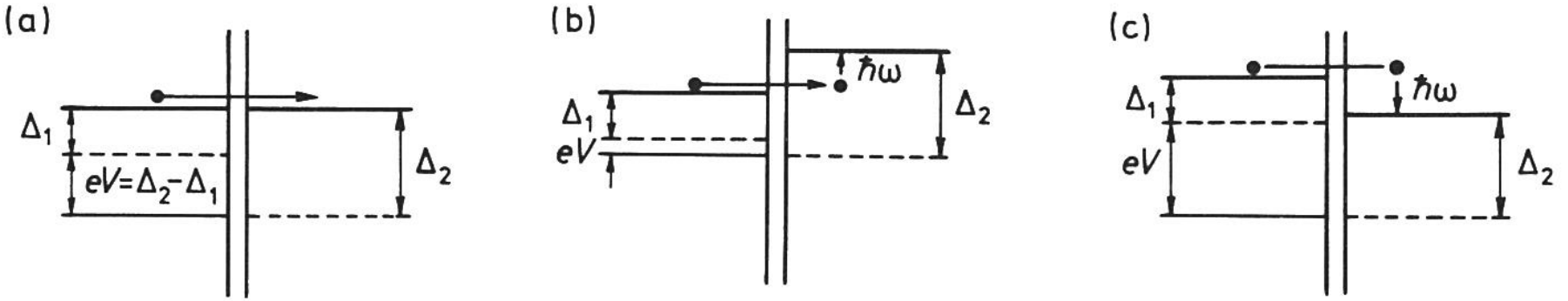

Fig. 5.8 Tunnelling between maximum density states at finite temperature (*a*) directly, (*b*) by photon absorption, (*c*) by photon emission.

The first experiments on tunnel junctions in the presence of electromagnetic waves were performed by Dayem and Martin [57] using junctions between Al and Pb, In or Sn. The frequency of the electromagnetic wave employed was 38·83 GHz so the experimental solution was to place the sample inside a cavity. The current–voltage characteristic was measured and rises in current were indeed found as may be seen in Fig. 5.9 (*a*) where the solid and dotted lines show the characteristic in the absence and presence of microwaves respectively.

Quantitative explanations were given nearly simultaneously by Tien and Gordon [58] and Cohen, Falicov and Phillips [126]. The methods in their papers were different but obtained essentially the same results. Cohen, Falicov and Phillips assumed that the magnetic field of the microwaves modulates the energy gap, whereas Tien and Gordon added an electrostatic perturbation term to the Hamiltonian. We shall follow here the latter derivation.

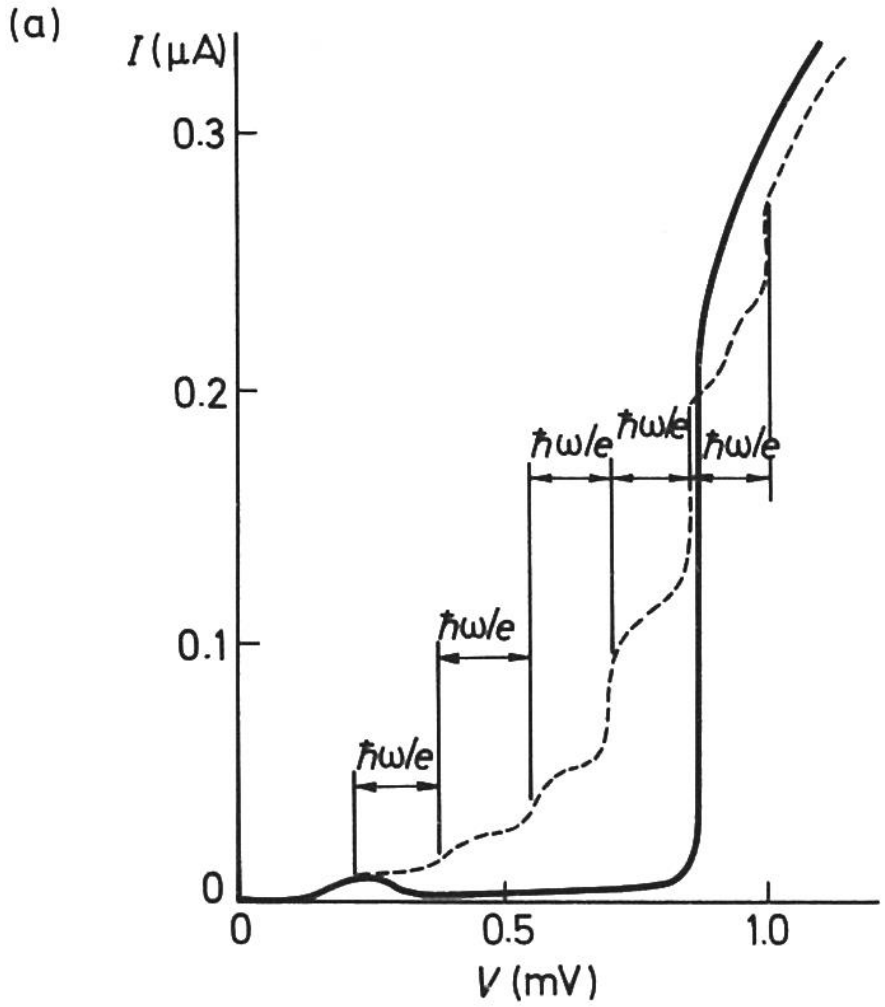

Fig. 5.9 (*a*) *I–V* characteristic of an Al–I–In junction in the absence (solid lines) and presence (dotted lines) of microwaves of frequency 38·83 GHz. Measurements by Dayem and Martin, quoted by Tien and Gordon [58].

The simplest assumption one can make is to regard the junction as a capacitance with a time-varying but spatially constant electric field between the plates. Regarding the potential of one of the superconductors (2) as the reference we may argue that the only effect of the microwave field is to add an electrostatic potential of the form

$$V_{\mathrm{rf}} \cos \omega t \tag{5.5}$$

to the energy of the electrons in the other superconductor (1). Hence, for electrons in superconductor (1) we may use the new Hamiltonian

$$H = H_0 + eV_{\mathrm{rf}} \cos \omega t \tag{5.6}$$

where the first term is the unperturbed Hamiltonian in the absence of microwaves.

If the unperturbed wavefunction was

$$\Psi_0(x, y, z, t) = f(x, y, z) \exp(-iEt/\hbar) \tag{5.7}$$

then the solution for the new wavefunction may be sought in the form

$$\Psi(x, y, z, t) = \Psi_0(x, y, z, t) \sum_{n=-\infty}^{\infty} B_n \exp(-in\omega t). \tag{5.8}$$

Substituting Equation (5.8) into Schrödinger's equation

$$H\Psi = i\hbar\frac{\partial\Psi}{\partial t} \tag{5.9}$$

we find

$$2nB_n = \frac{eV_{\mathrm{rf}}}{\hbar\omega}(B_{n+1} + B_{n-1}) \tag{5.10}$$

which is satisfied by [101]

$$B_n = J_n(eV_{\mathrm{rf}}/\hbar\omega) \tag{5.11}$$

where J_n is the n_{th} order Bessel function of the first kind. The new wavefunction is then

$$\Psi(x, y, z, t) = f(x, y, z, t)\exp(-iE\hbar/t)\sum_{n=-\infty}^{\infty} J_n(\alpha)\exp(-in\omega t), \tag{5.12}$$

where

$$\alpha = \frac{eV_{\mathrm{rf}}}{\hbar\omega}. \tag{5.13}$$

It may be seen that in the presence of microwaves the wavefunction contains components with energies

$$E, E \pm \hbar\omega, E \pm 2\hbar\omega, \ldots \tag{5.14}$$

respectively. Without the electric field, an electron of energy E in superconductor (1) can only tunnel to the states in superconductor (2) of the same energy. In the presence of the electric field, the electron may tunnel to the states in superconductor (2) of energies E, $E \pm \hbar\omega$, $E \pm 2\hbar\omega$, etc. Let $N_{20}(E)$ be the unperturbed density of states of the superconductor (2). In the presence of microwaves we then have an effective density of states given by

$$N_2(E) = \sum_{n=-\infty}^{\infty} N_{20}(E + n\hbar\omega) J_n^2(\alpha). \tag{5.15}$$

We may now obtain the tunnelling current by substituting Equation (5.15) into the general expression Equation (2.14), yielding*

The tunneling current equation, Solymar (2.14)

$$I = A \sum_{n=-\infty}^{\infty} J_n^2(\alpha) \int_{-\infty}^{\infty} N_1(E-eV) N_{20}(E+n\hbar\omega)\left[f(E-eV)-f(E+n\hbar\omega)\right] dE$$

$$= A \sum_{n=-\infty}^{\infty} J_n^2(\alpha) I_0(eV+n\hbar\omega) \qquad (5.16)$$

where $I_0(eV)$ is the tunnelling current in the absence of microwaves.

In the limit $\hbar\omega \to 0$ it may be shown (see Appendix 5) that the above expression reduces to the classical value

$$I = \frac{1}{\pi} \int_{-\pi/2}^{\pi/2} I_0(V + V_{\mathrm{rf}} \sin \omega t)\, d(\omega t). \qquad (5.17)$$

The comparison between theory and experiments has a long and tangled story. The first attempt was made by Tien and Gordon [58] who could reproduce the experimental results of Dayem and Martin [57] by taking $\alpha = 2$ as shown in Fig. 5.9 (*b*). The experimental value of α (that is the voltage in the junction) was, however, not known. Estimates by Tien and Gordon indicated a discrepancy as large as an order of magnitude.

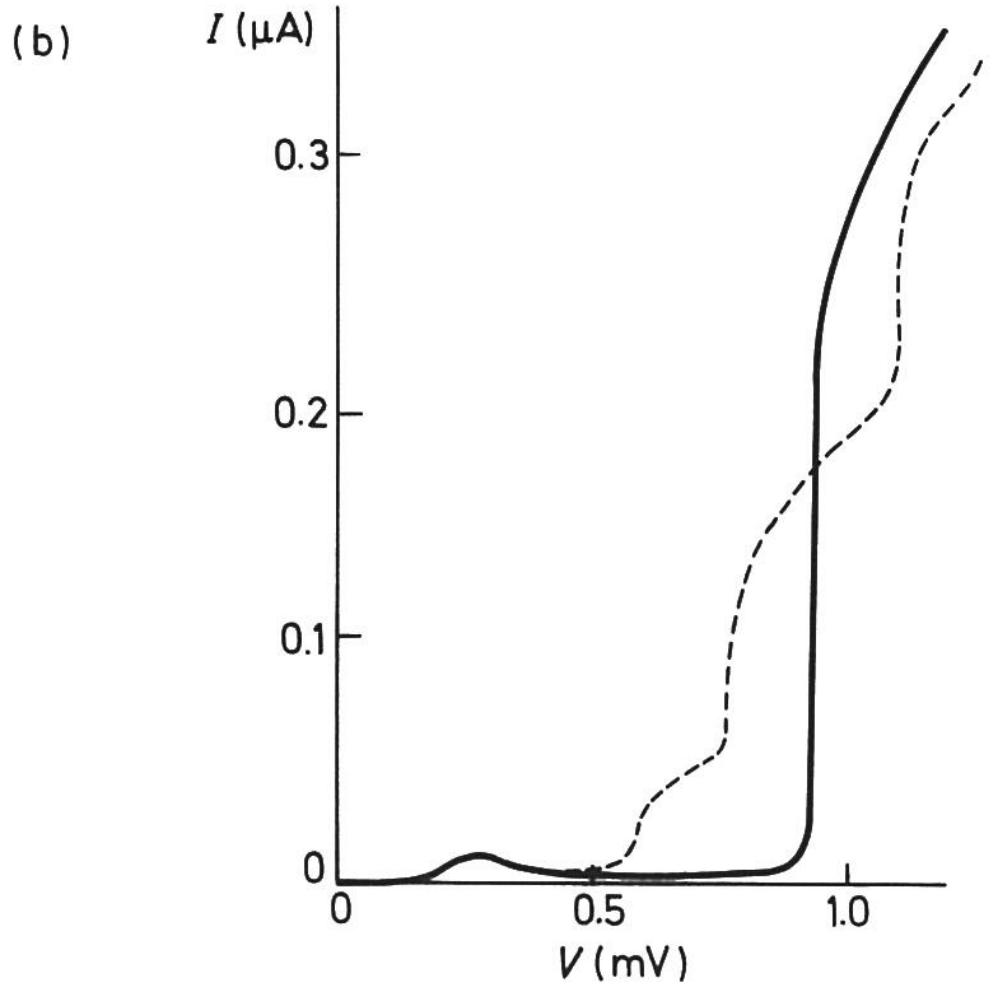

Fig. 5.9 (*b*) Theoretical curves by Tien and Gordon [58] for $\alpha = 2$.

To prove the point that it is the spatial variation which is responsible for the discrepancy, Hamilton and Shapiro [135] conducted another series of experiments on a very small (hardly overlapping in an in-line geometry) junction. The results then did agree with the Tien–Gordon theory as shown in Fig. 5.15.

Two more proofs in favour of the Tien–Gordon theory are the measurements of Hamilton and Shapiro [135] at 200 Hz where V_{rf} could be easily measured and the microwave experiments of Longacre and Shapiro [137] conducted on point contact (that is, very small) junctions.

Shapiro steps in the n^{th} order, observed in very small junctions

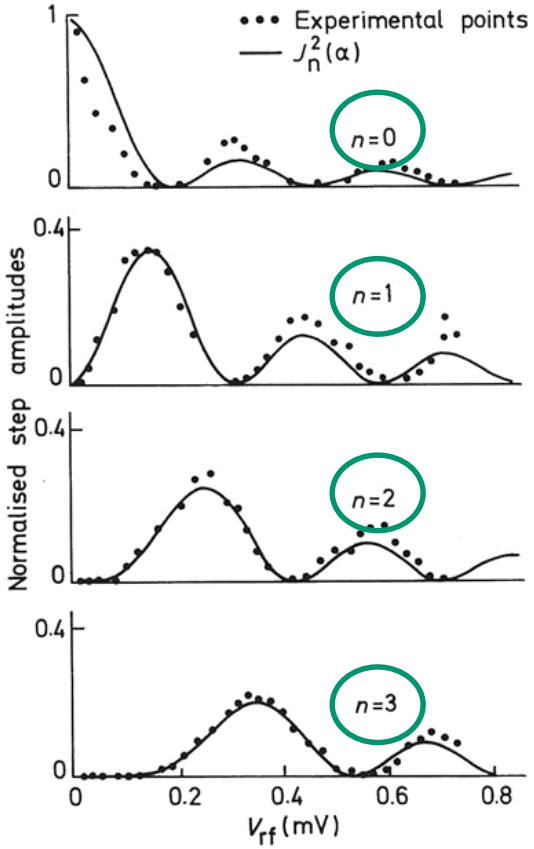

Fig. 5.15 Same as Fig. 5.14 for a very small junction. After Hamilton and Shapiro [135].

Observations of quasi-particle tunneling and Josephson behavior in $Y_1Ba_2Cu_3O_{7-x}$/native barrier/Pb thin-film junctions

J. Kwo, T. A. Fulton, M. Hong, and P. L. Gammel
AT&T Bell Laboratories, Murray Hill, New Jersey 07974

(Received 4 December 1989; accepted for publication 20 December 1989)

Low-leakage, thin-film planar tunnel junctions made of $Y_1Ba_2Cu_3O_{7-x}$/native barrier/Pb were fabricated. The $Y_1Ba_2Cu_3O_{7-x}$ films were prepared by *in situ* molecular beam epitaxy aided with an activated oxygen source. The as-grown, smooth superconducting perovskite film surface exhibits quasi-particle tunneling characteristics very similar to the etched bulk single-crystal data. The results in agreement are a linear dependence of the normal-state conductance on voltage, a gap-like structure at $\sim$20 mV, asymmetric modulations up to 50 mV, and a finite zero-bias conductance at low temperature. Junctions of lower resistance show, at temperatures below T_c of Pb, the development of a supercurrent at zero bias and associated hysteretic subgap structure, with a typical $I_cR \sim 0.5$ mV. Josephson-like behavior occurred in response to applied magnetic field and microwaves.

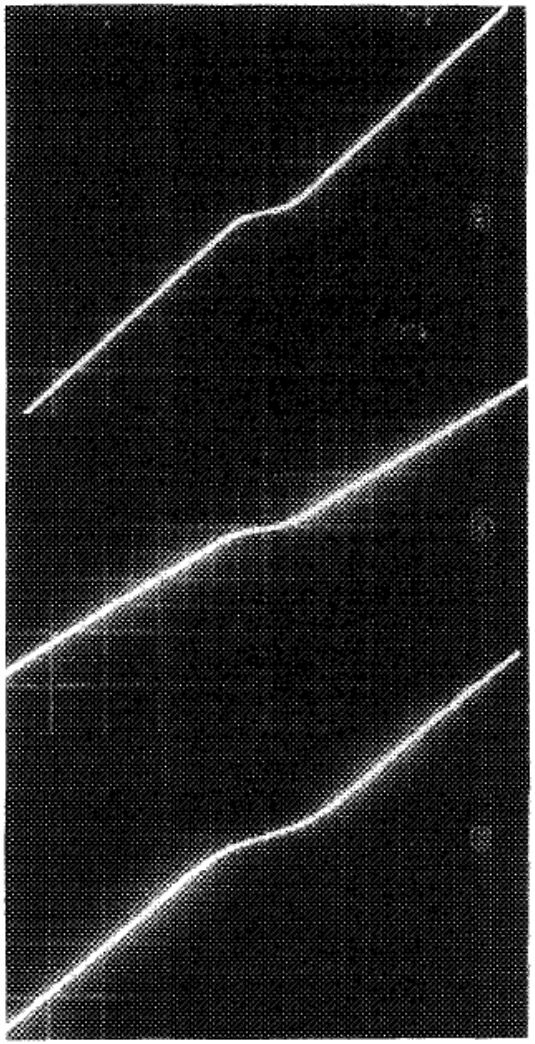

FIG. 1. Current-voltage characteristics for junctions (a), (b), and (c) at 4.2 K. The x axis (voltage) scales are 2, 2, and 1 mV per large division (pld) for (a), (b), and (c), respectively. The y axis (current) scales are 100, 250, and 250 μA pld for (a), (b), and (c), respectively.

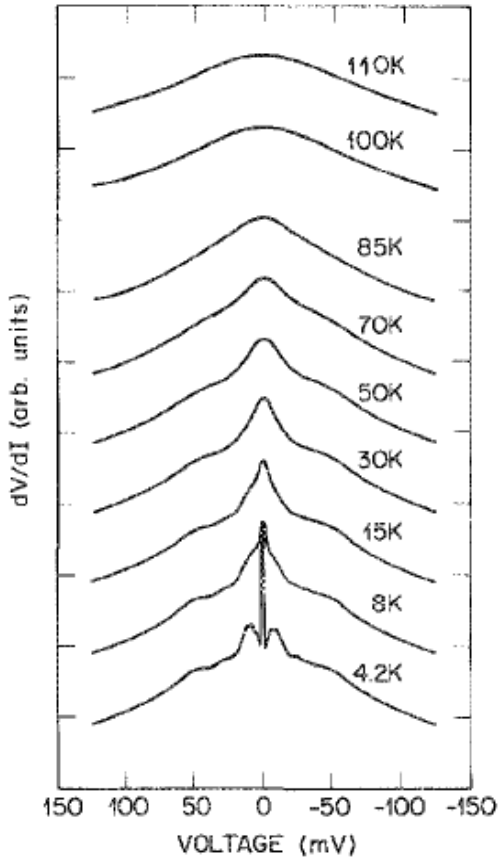

FIG. 2. Dynamic resistance $R(V)$ vs V as a function of temperature below and above T_c of a $Y_1Ba_2Cu_3O_{7-x}$ film. The zero of $R(V)$ at 4.2 K is on the base line, and the zeros of other traces are displaced progressively by one division.

Josephson current

1. Single slit diffraction pattern under B field
2. Shapiro steps in AC microwaves

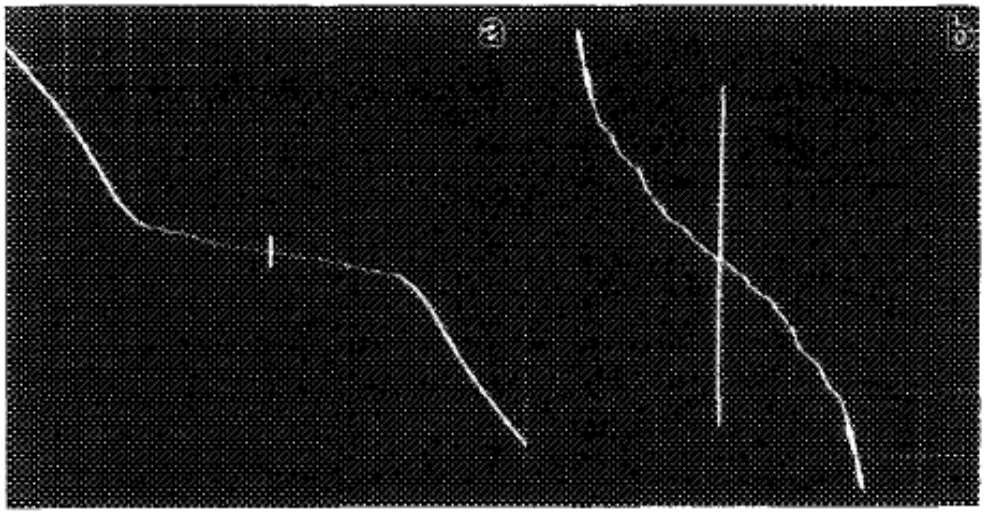

FIG. 3. Supercurrent and assoicated subgap structure at 1.5 K of a junction of R(10 mV) of 80 Ω. The x axis scale is 0.5 mV pld for (a) and (b). The y axis is (a) 10 μA pld and (b) 2 μA pld.

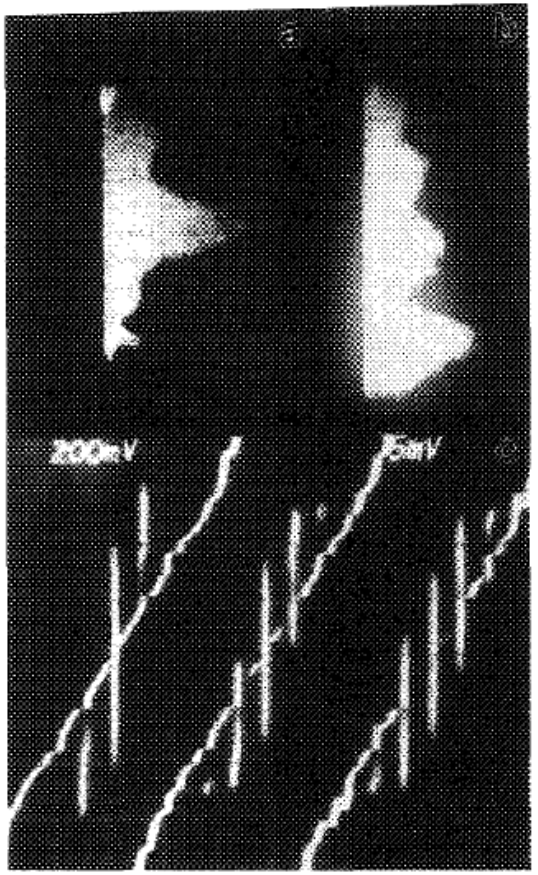

FIG. 4. Critical current (x axis, 1 μA pld) vs applied magnetic field (y axis, 1.9 G pld) for B swept (a) from negative to positive values and (b) in the opposite sense. The junction is in the $V = 0$ state where the trace is bright. (c) Occurrence of Shapiro current steps in the I-V in response to applied microwaves of 11.9 GHz. X scale is 50 μV pld and Y scale is 0.2 μA pld. Applied power is zero, intermediate, and full from left to right. The sloping steps on the leftmost trace are geometrical resonances. Shapiro steps up to $n = 2$ are visible in the right trace.

6.9 Strong coupling superconductors

The most convincing proof of the validity of the BCS theory came from tunnelling measurements but it became clear from the same measurements that some superconductors behaved somewhat differently. Giaever and Megerle [69] observed that the temperature dependence of the energy gap of lead obeyed the BCS theory only if they used the experimentally obtained value of $\Delta(0)$. The ratio $2\Delta(0)/kT_c$ was found to be 4·3, well above the BCS value of 3·52. A year later Giaever, Hart and Megerle [66] found a small but significant deviation from the BCS density of states when plotting $\sigma(V)$ as shown in Fig. 6.18. The crossover point is at about $k\theta_D$ the Debye energy suggesting immediately (low Debye energy implies strong electron–phonon interaction) the cause and the direction in which the BCS theory should be modified. In fact, more general theories were already available. Eliashberg [68] had already derived his gap equation taking into account both the electron–phonon matrix element and the phonon spectrum, but before the strategic attack upon this equation a number of tactical advances were necessary to make it sure that the experimental results were in line with the theoretical predictions. The story of these efforts is reviewed by Rowell and McMillan [165]; we shall briefly outline here the major steps in the process.

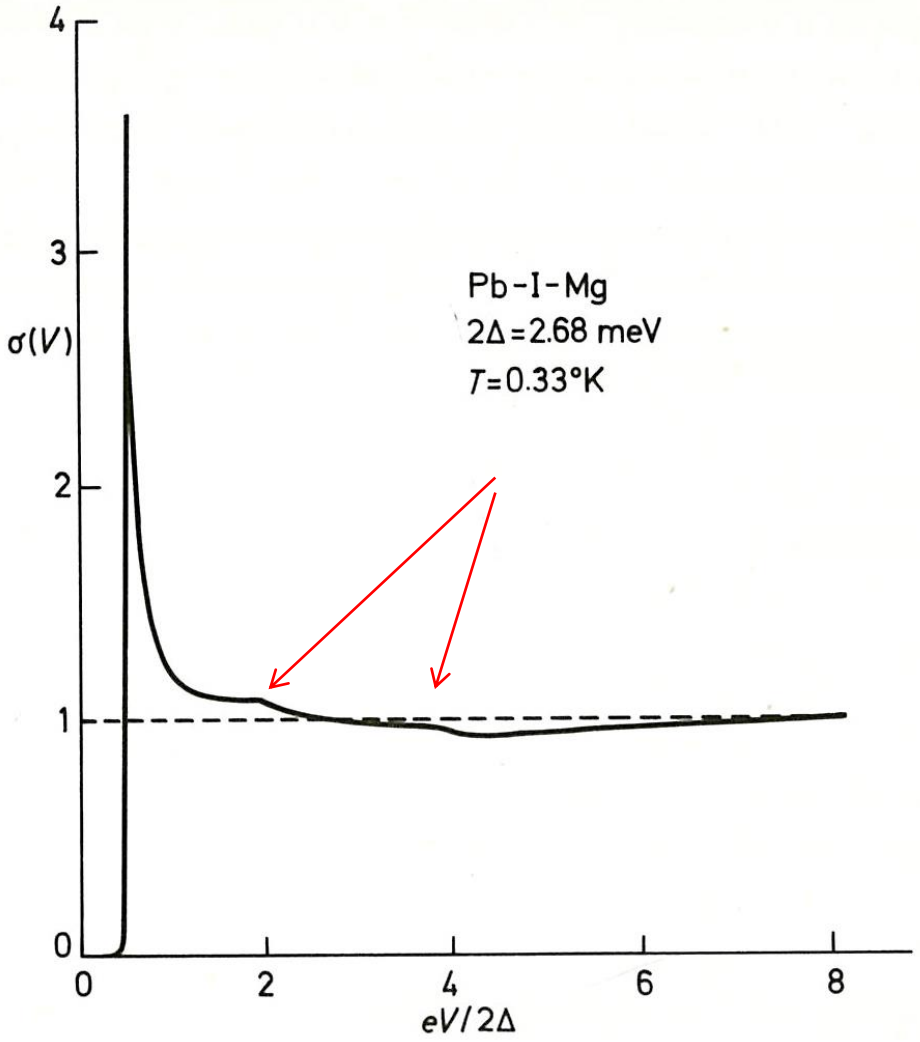

Fig. 6.18 Normalised differential conductance as a function of normalised voltage for a Pb–I–Mg junction. The structure shown in the curve signifies deviation from the BCS theory. The cross-over point corresponds to the Debye energy. After Giaever, Hart and Megerle [66].

Electron-Phonon Interaction by Tunneling Spectroscopy

William McMillan

John Rowell

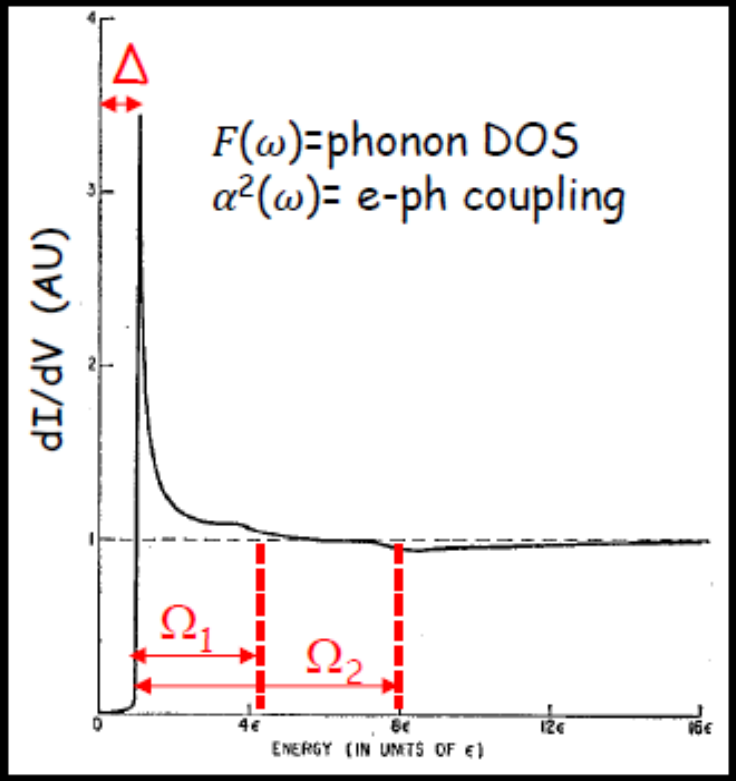

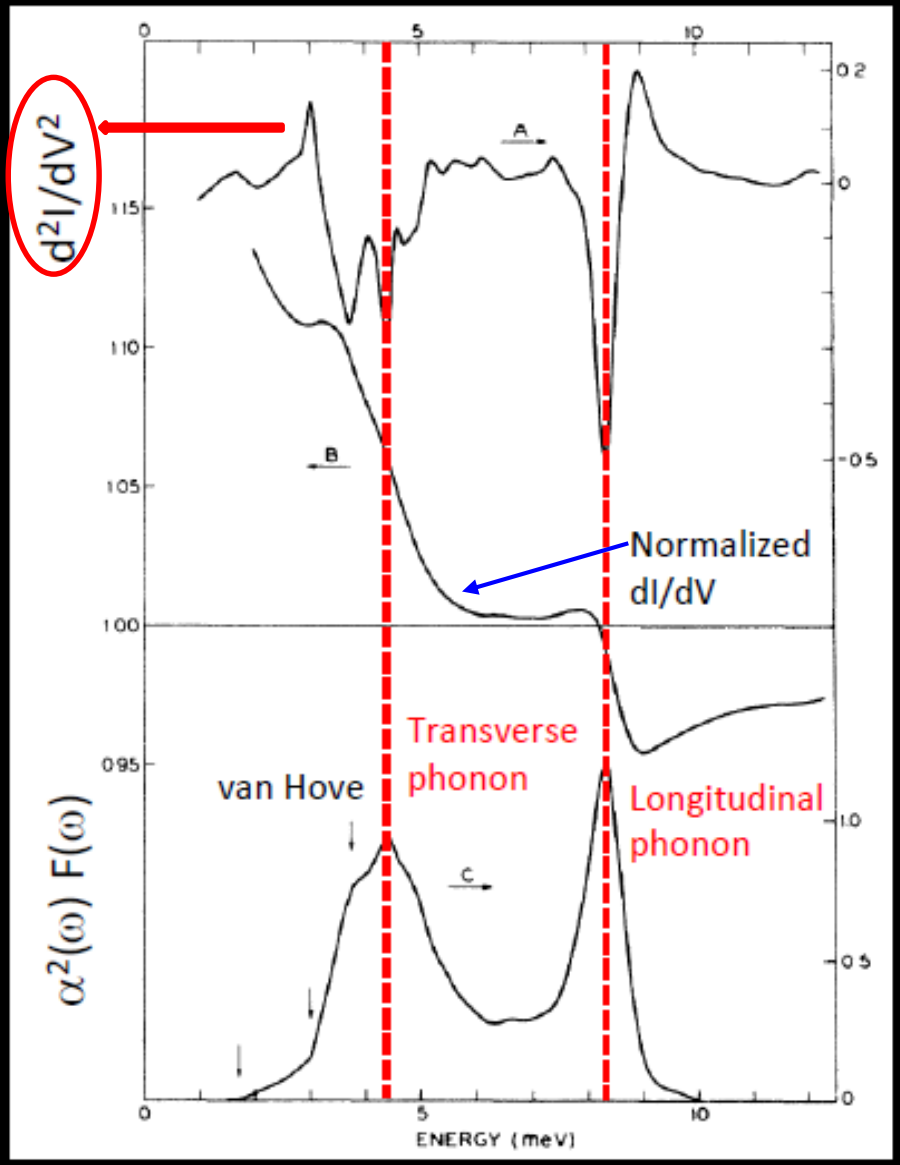

W.L. McMillan & J.W. Rowell, PRL 14, 108 (1965)

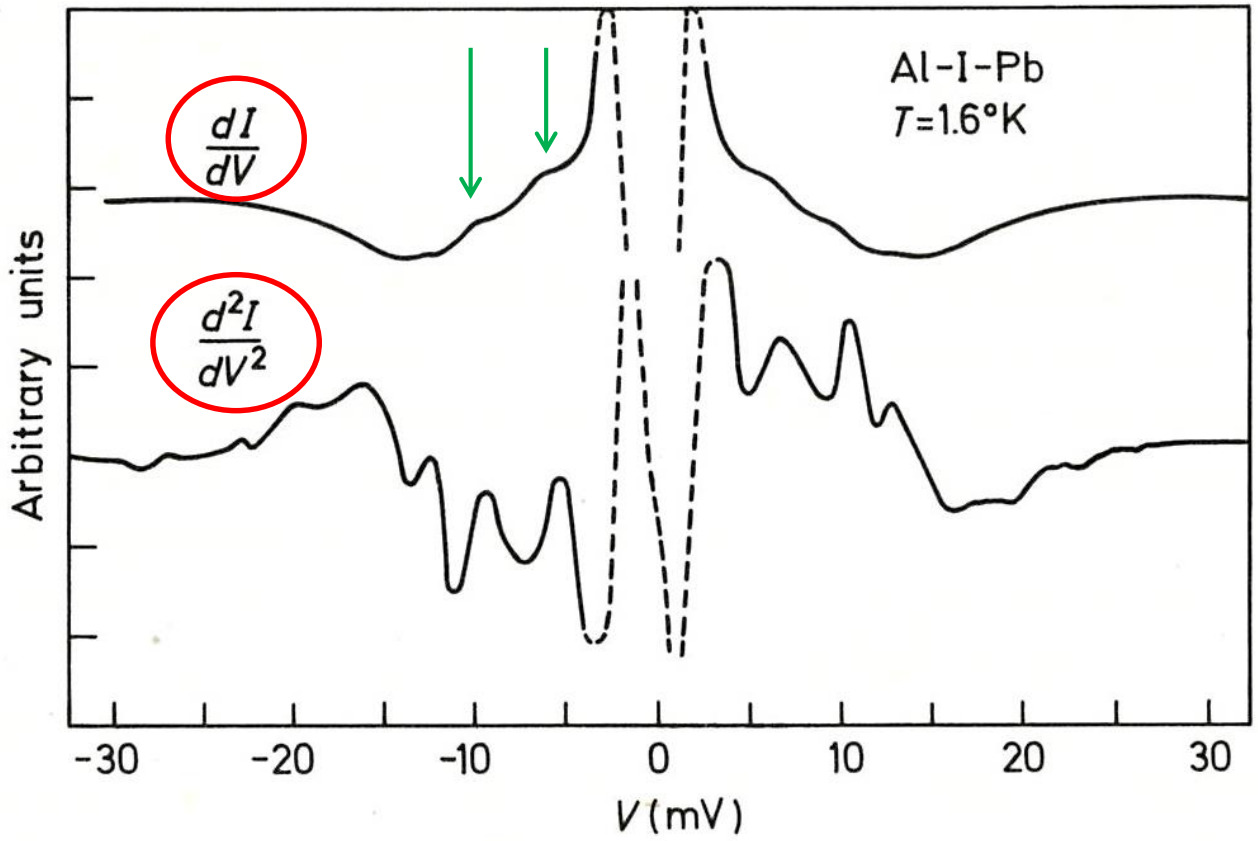

Fig. 6.19 First and second derivatives of the I–V characteristic as a function of voltage for an Al–I–Pb junction. After Rowell, Chynoweth and Phillips [219].

Morel and Anderson [218] approximated the effective phonon density by an Einstein peak at the longitudinal phonon frequency ω_L and predicted structure in the tunnelling density of states at energies $n\hbar\omega_L$. Subsequent measurements by Rowell *et al.* [219] (on Al–I–Pb junctions at 1·6°K) of the second derivative of the I–V characteristic did indeed produce the expected structure as shown in Fig. 6.19. The peak positions are given empirically by the formula

$$E_n = \Delta^1 + n\theta \tag{6.2}$$

where Δ^1 agrees roughly with the value for half the energy gap and $\theta = 3{\cdot}7$ meV is in the range of appreciable transverse phonon energies measured by neutron diffraction.

A refinement of the theory by Schrieffer *et al.* [220] was matched by further refinement of the experimental techniques [221]. By assuming the phonon density in the form of two Lorentzian peaks (representing the transverse and longitudinal phonons respectively) shown in Fig. 6.20 (*b*) and taking reasonable

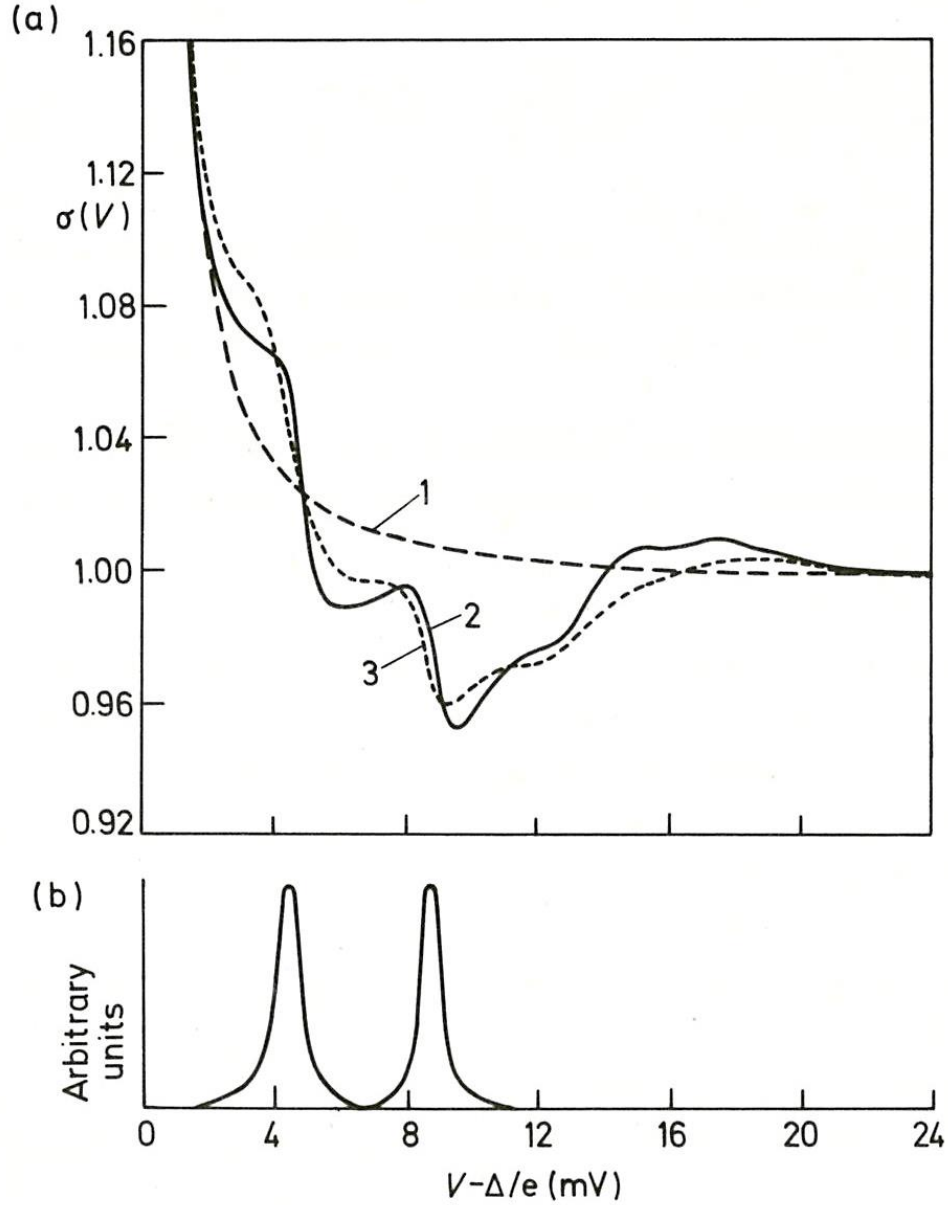

Fig. 6.20 (*a*) The normalised differential conductance as a function of voltage (zero shifted by Δ/e), 1 : BCS theory, 2 : theory by Schrieffer *et al.* [220], 3 : experimental results by Rowell, Anderson and Thomas [221]. (*b*) The phonon spectrum assumed by Schrieffer *et al.* [220].

values for α the electron–phonon coupling and μ^* the Coulomb pseudo-potential (a parameter entering the Eliashberg gap equation) a theoretical curve was obtained for $\sigma(V)$ in excellent agreement with tunnelling data (Fig. 6.20 (*a*)). Second derivative measurements [221] (Fig. 6.21) did in fact show considerably more structure for which the theory of Schrieffer *et al.* [220] could not account. These came to be identified with Van Hove singularities* measured by neutron diffraction [222]. Although the relationship of this last structure to the density of states was explained by Scalapino and Anderson [223] the conviction grew that a frontal assault on the Eliashberg equation had become feasible.

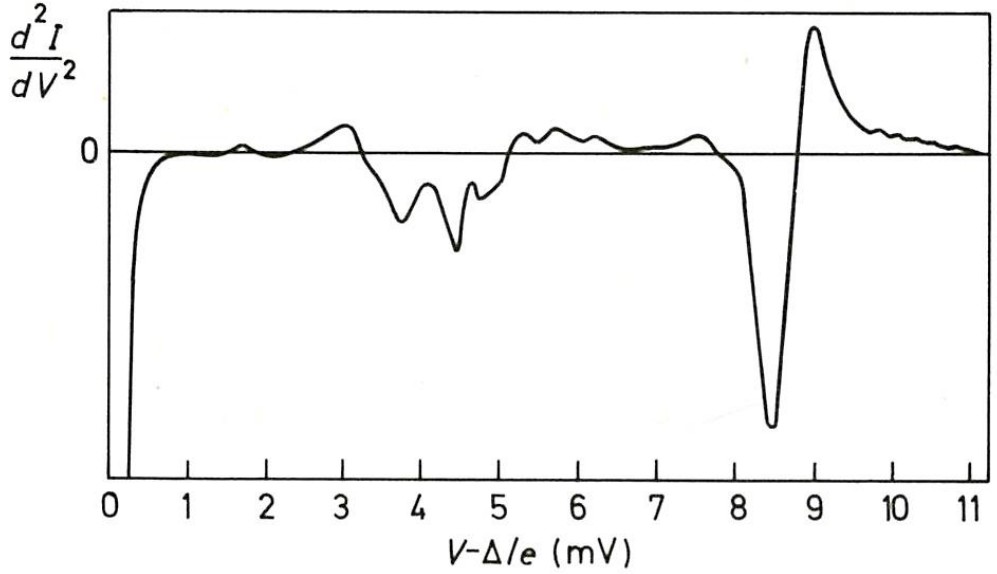

Fig. 6.21 The second derivative of the I–V characteristic as a function of voltage (zero shifted by Δ/e). Arrows indicate the voltage for Van Hove singularities on the basis of the neutron diffraction experiments of Brockhouse *et al.* [222]. After Rowell, Anderson and Thomas [221].

The method used by McMillan and Rowell [67] is based on the fact that in Eliashberg's theory the electron–phonon coupling constant weighted by the phonon density of states $\alpha^2(\omega)F(\omega)$ is uniquely related to the electronic density of states (as measured by tunnelling experiments). Hence besides working out the density of states from phonon data it is also possible to invert the Eliashberg equation and get the phonon data from the measured tunnelling characteristics. With the aid of a computer $\alpha^2(\omega)F(\omega)$ and μ^* are adjusted until the computed density of states accurately fits the measured density of states for $E < k\theta_D$. Examining the agreement for $E > k\theta_D$ the accuracy of the Eliashberg equation can be tested. The results of this rather difficult exercise may be seen in Fig. 6.22 where theory and experiments are compared. The experimental points below $E - \Delta = 11$ meV were used for determining the 'input' quantities, and the points above that are to be compared with the theory. It is remarkable that an experimental curve as complicated as that can be theoretically reproduced. McMillan and Rowell [166] conclude that our present theories of superconductivity are accurate to a few percent.*

All the experiments mentioned so far were concerned with the properties of lead. The other strong-coupling superconductor, mercury (with $2\Delta/kT_c = 4{\cdot}6$), was less thoroughly investigated but the available data [225–226] suggest similar conclusions.

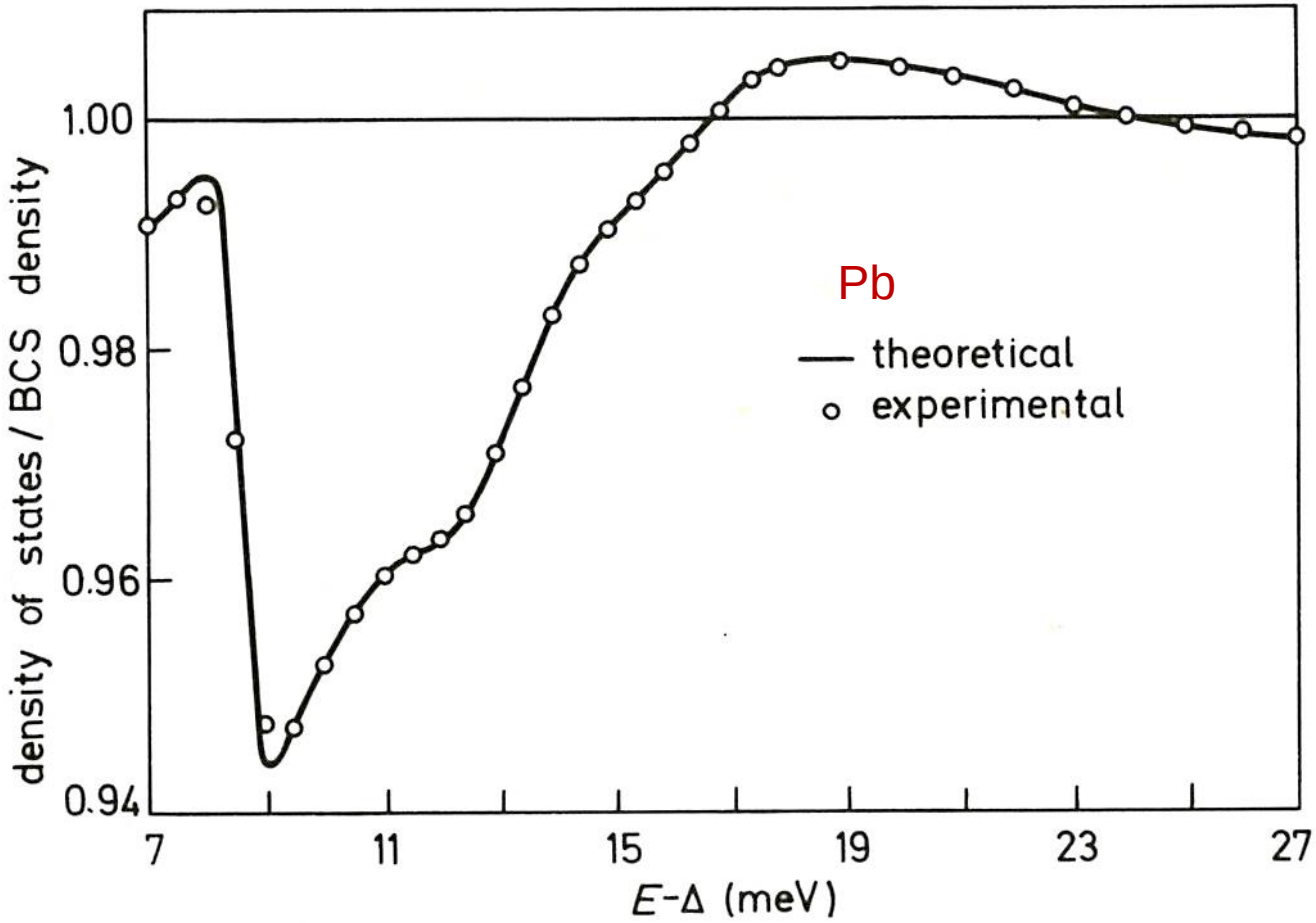

Fig. 6.22 The density of states for lead related to the BCS density of states as a function of energy (zero shifted by Δ). In the experiment the sharp drop near 9 meV is affected by thermal smearing. After McMillan and Rowell [165].

Next we shall briefly review the tunnelling experiments on lead-based alloys. The effect of a small amount of indium on the phonon spectrum was investigated by Rowell, McMillan and Anderson [227] using the inversion technique described above. The results for $\alpha^2(\omega)F(\omega)$ are shown in Fig. 6.23. The additional structure at $\hbar\omega = 9{\cdot}5$ meV is due to the presence of an 'impurity band'.** The impurity band is still present at higher indium concentrations as reported by Adler *et al.* [228]. The value of $2\Delta/kT_c$ slowly decreases with increasing indium concentration; it is 4·34 at 2 atomic percent indium reducing to 4·20 at 70 atomic percent indium.

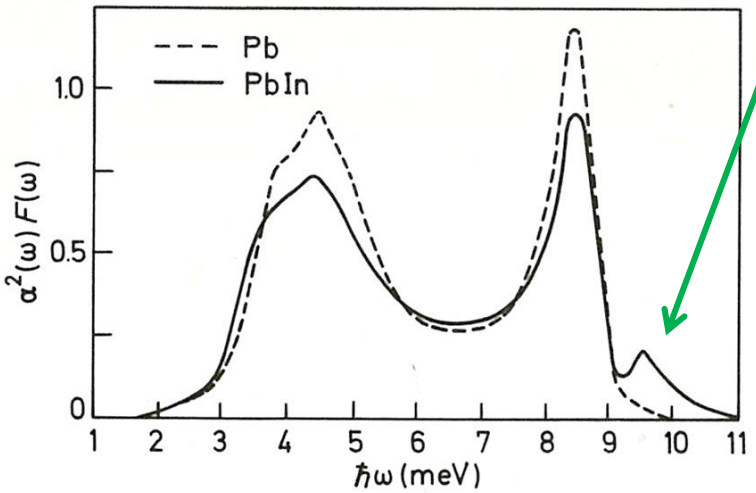

Fig. 6.23 The phonon spectrum $\alpha^2(\omega)F(\omega)$ obtained by the gap inversion technique. The localised phonon mode of the light indium impurity may be seen at about 9·5 meV. After Rowell, McMillan and Anderson [227].

Superconducting Weak Links

Summarising, the present state of affairs is that besides thin tunnel junctions and point contacts, discussed in connection with normal electron tunnelling, we have some other geometries as well displaying the characteristic effects (like induced steps in the I–V characteristics, quantum interference, radiation, etc.).

The various geometries are shown in Fig. 8.6. The superconducting thin film bridge (Fig. 8.6 (a)) was developed by Dayem and it is often referred to as the Dayem bridge. It consists essentially of a narrow constriction of the order of $(1\ \mu\text{m})^2$ between two superconducting films.

A variation of the thin film bridge is the Notarys bridge [363] shown in Fig. 8.6 (b). This relies on the proximity effect to cause weak superconductivity. There is first a layer of normal metal evaporated, and then the superconductor forming the bridge. The 'weakness' is controlled by the relative thicknesses of the normal and superconducting layers.

The solder junction (Fig. 8.6 (c)) was developed by Clarke [338]. It is very simple to make; one simply has to dip a piece of oxidised wire into molten solder. When the solder freezes tight mechanical contact is established and the junction is ready. Its disadvantage is that the junction is not clearly defined.

The point contact junction is also widely used but not necessarily in the same form as for single particle tunnelling. Then the presence of the insulating layer is essential for displaying tunnelling characteristics. The Josephson effects may, however, be observed whether there is an insulating layer or not. If the two superconductors are in contact then we have a bridge. In actual experiments very often we do not even know whether we have a weak link or a tunnel junction. Take for example the point contact junctions developed by Zimmerman and Silver [341]. They used superconducting screws with lock nuts pressed against a superconducting surface through a Mylar spacer (Fig. 8.6 (*d*)). There is no way of knowing whether there is a direct contact between the superconductors or not. All the measurements can tell us is that there is a difference in the I–V characteristics (the increase in the maximum supercurrent can be clearly observed) as more pressure is applied, leading eventually to a 'strong link', i.e. a proper short-circuit.

Weak Links

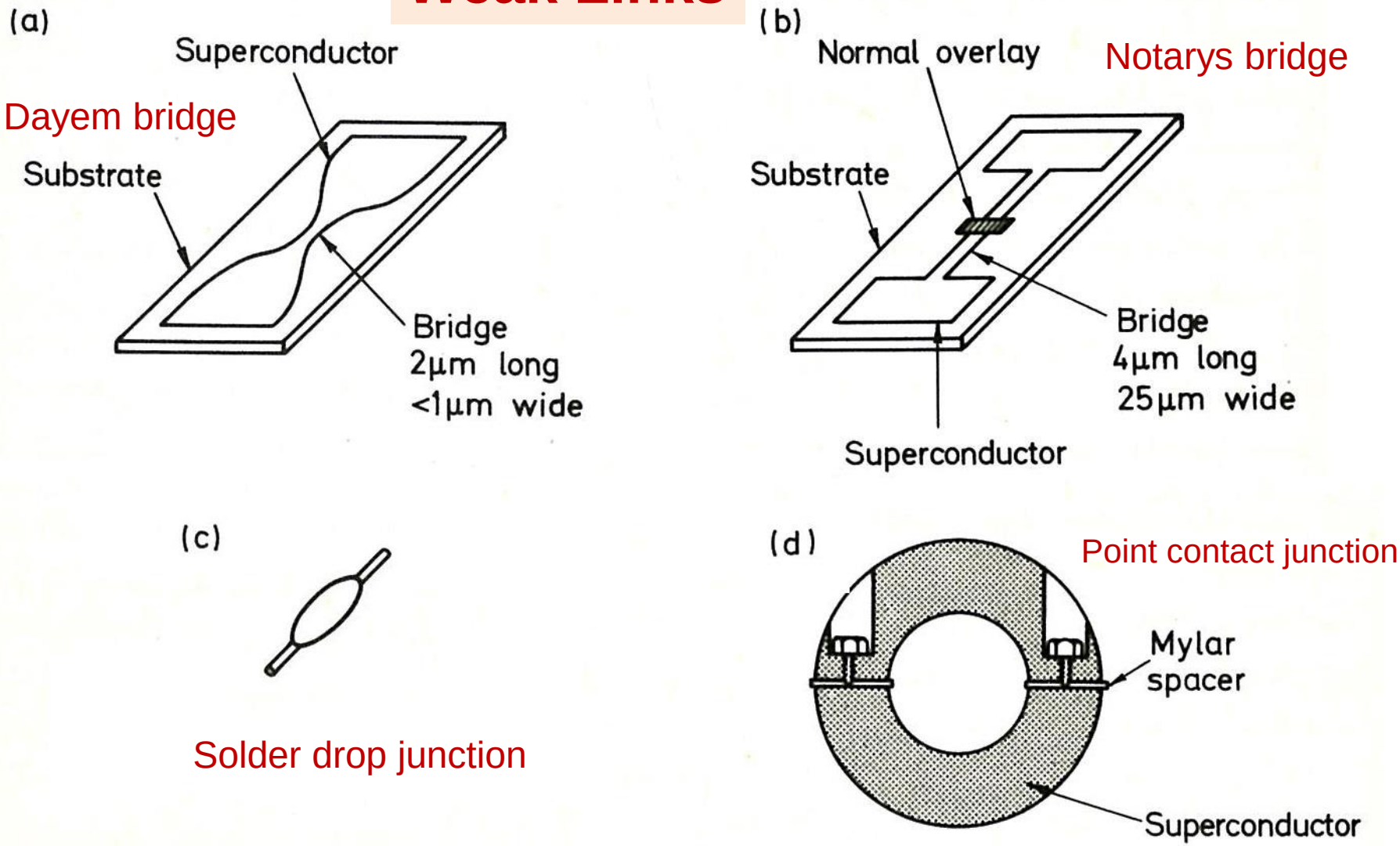

Fig. 8.6 Weak links exhibiting properties similar to those of Josephson junctions. (*a*) A superconducting thin film bridge (Dayem bridge), (*b*) a superconducting thin film bridge with a normal metal overlay (Notarys bridge), (*c*) Clarke's solder drop junction (*d*) double point-contact junction developed by Zimmerman and Silver [341].

Let us discuss now briefly that in what sense does a weak link resemble to a tunnel junction. There is no difficulty as far as the d.c. Josephson effect is concerned. At low currents there is no voltage across the weak link but as the current is increased the weak link will first turn resistive. This is because it has a smaller cross-section and thus a higher current density or (as in the Notarys bridge) it has a lower critical temperature. So we may say that it is true both for tunnel junctions and for weak links that there is no voltage up to a certain current and finite voltage above a certain current.

It is somewhat more difficult to envisage the a.c. effects. We can no longer appeal to the simple physical picture that the tunnelling Cooper pairs radiate out their energy. There is though a simple heuristic argument (due to Mercereau [364]) which can justify the presence of an a.c. supercurrent. The argument (in an abbreviated form) runs as follows.

A voltage across the weak link will effect both the normal and the superconducting electrons. The superconducting electrons will be accelerated according to Newton's Law

$$\frac{dv}{dt} = \frac{q}{m}\mathscr{E} \tag{8.7}$$

where the electric field $\mathscr{E}$ is sustained by the normal electrons. It is known, however, that when the superconducting electrons reach a certain velocity (say v_c) their density vanishes. But then there is only an electric field across the weak link which on its own cannot quench superconductivity; hence the superconducting electrons reappear and the whole process repeats itself.

Let us now make a rough calculation of the time needed to accelerate the superconducting electrons to a velocity v_c. For a constant $\mathscr{E}$ we get

$$\tau = \frac{mv_c}{q\mathscr{E}}. \tag{8.8}$$

Assuming that the electric field is constant over one coherence length (the shortest distance over which the density of superconducting electrons can change), the voltage across this region is given by

$$V = \mathscr{E}\xi \tag{8.9}$$

Expressing further the final momentum in terms of the coherence length by the relation

$$mv_c = \frac{h}{\xi} \tag{8.10}$$

where mv_c is the uncertainty in momentum, we get

$$\tau = \frac{h}{qV}$$

for the period of this 'relaxation oscillation'. Hence the angular frequency is

$$\omega = \frac{qV}{\hbar} \tag{8.11}$$

which agrees with Equation (8.3). So we managed to show (by hook or by crook) that weak links have the same radiation properties as tunnel junctions. In fact, the difference between tunnel junctions and weak links is not so much in the basic processes but rather in the circuits they represent to the outside world.

For most purposes a junction may be adequately represented by the parallel combination of an 'ideal' junction (one which carries a supercurrent only) a resistance and a capacitance. The main differences between tunnel junctions, point contacts and bridges are in the respective values of these circuit elements.

For a Josephson current of $I_J = 10\ \mu A$, the range for practical junctions is shown in Table 8.1 [365]. It is then obvious that, for example, for high frequency operation (microwaves or above) the point contact is superior to the tunnel junction. The relative values of the circuit elements play an important role in determining the I–V characeristics as well. This will be discussed in Chapter 11.

Table 8.1

	I_J	$1/G$ (*for* $V < 2\Delta$)	C
Thin film tunnel junction	10 μA	> 100 ohm	100 to 1000 pF
Point contact	10 μA	10 to 100 ohm	1 to 1000 pF
Thin film bridge	10 μA	< 1 ohm	1 pF

Circuit Representation

11.2 Capacitive loading; constant conductance

The circuit we are considering here (Fig. 11.1 (*a*)) consists of an ideal current generator feeding current into the parallel combination of a Josephson junction,

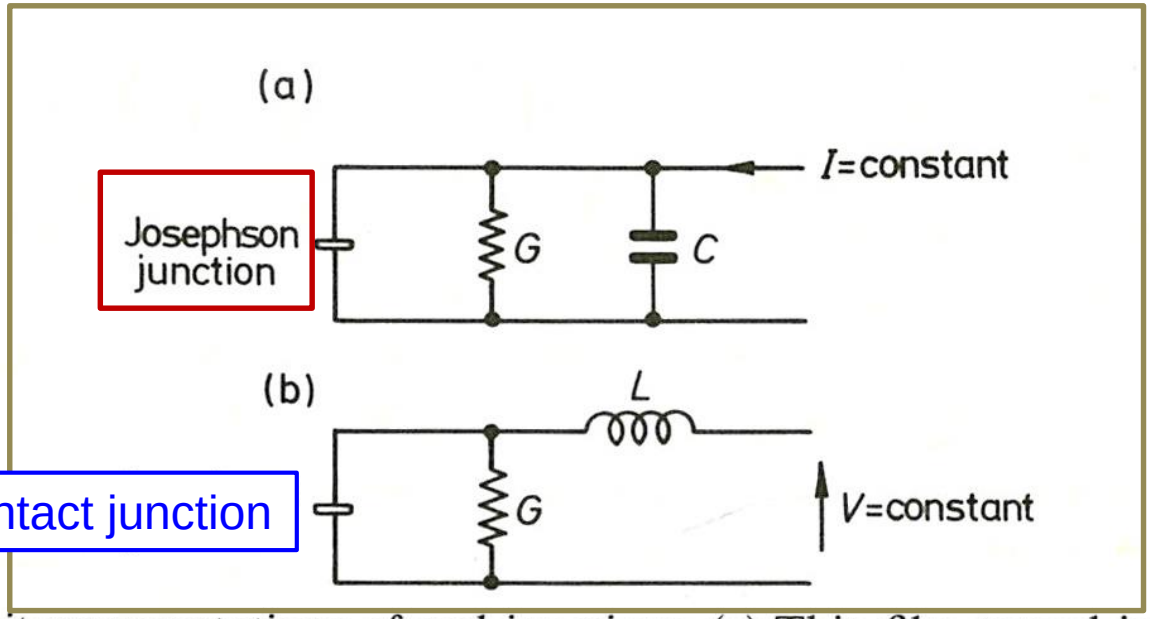

Fig. 11.1 Circuit representations of real junctions. (*a*) Thin film tunnel junction made up by an 'ideal' Josephson junction (satisfying the $I = I_J \sin\phi$ relationship), an ohmic conductance and a capacitance; analysed for a constant current input. (*b*) An approximation to a point-contact junction taking account of parallel conductance and series inductance; analysed for a constant voltage input.

an ordinary ohmic conductance and a capacitance. We have then a supercurrent

$$I_J \sin \phi \tag{11.1}$$

through the Josephson junction, an ohmic current

$$GV \tag{11.2}$$

through the conductance and a capacitive current

C= Q/V, Q =CV

$$C\frac{dV}{dt} \tag{11.3}$$

through the capacitance. The sum of these three components should be equal to I, the current supplied by the generator. This is not really new. We have met all these components of current before; taking the current (more correctly the current density) in the form of Equation (9.34) and adding the displacement current, we get an equation expressing the same relationship

$$I = I_J \sin \phi + GV + C\frac{dV}{dt}. \tag{11.4}$$

Expressing the voltage with the aid of the phase (Equation (9.17)) the above equation reduces to

$$I = \frac{\hbar C}{q}\frac{d^2\phi}{dt^2} + \frac{\hbar G}{q}\frac{d\phi}{dt} + I_J \sin \phi. \tag{11.5}$$

$\partial\phi/\partial t = qV/\hbar$

Scanning Tunneling Microscope (STM)

Heinrich Rohrer & Gerd Binnig (1983)

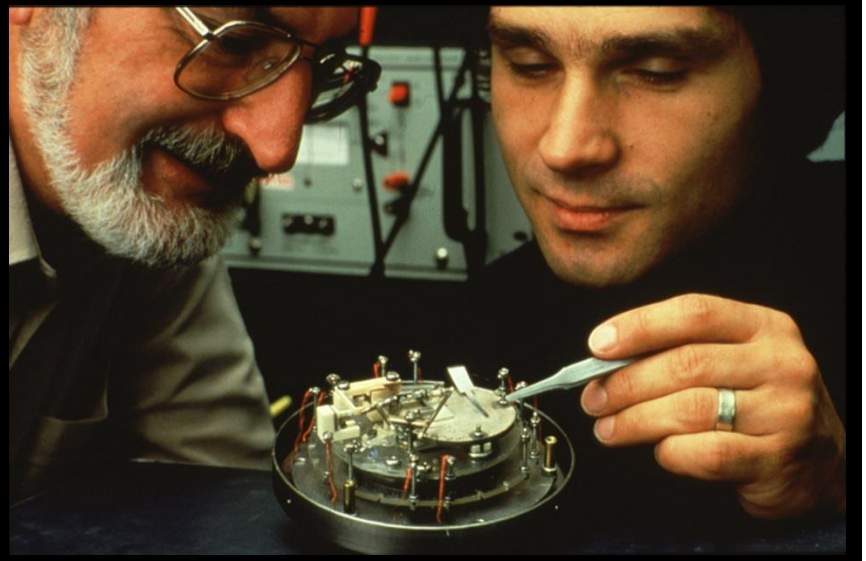

Nobel Prize in 1986 ©IBM, Zurich

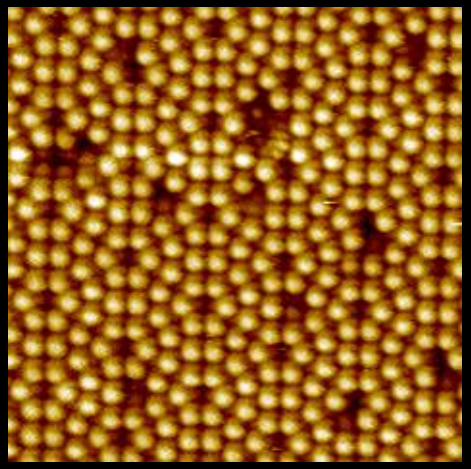

Si (111) surface 7 x 7

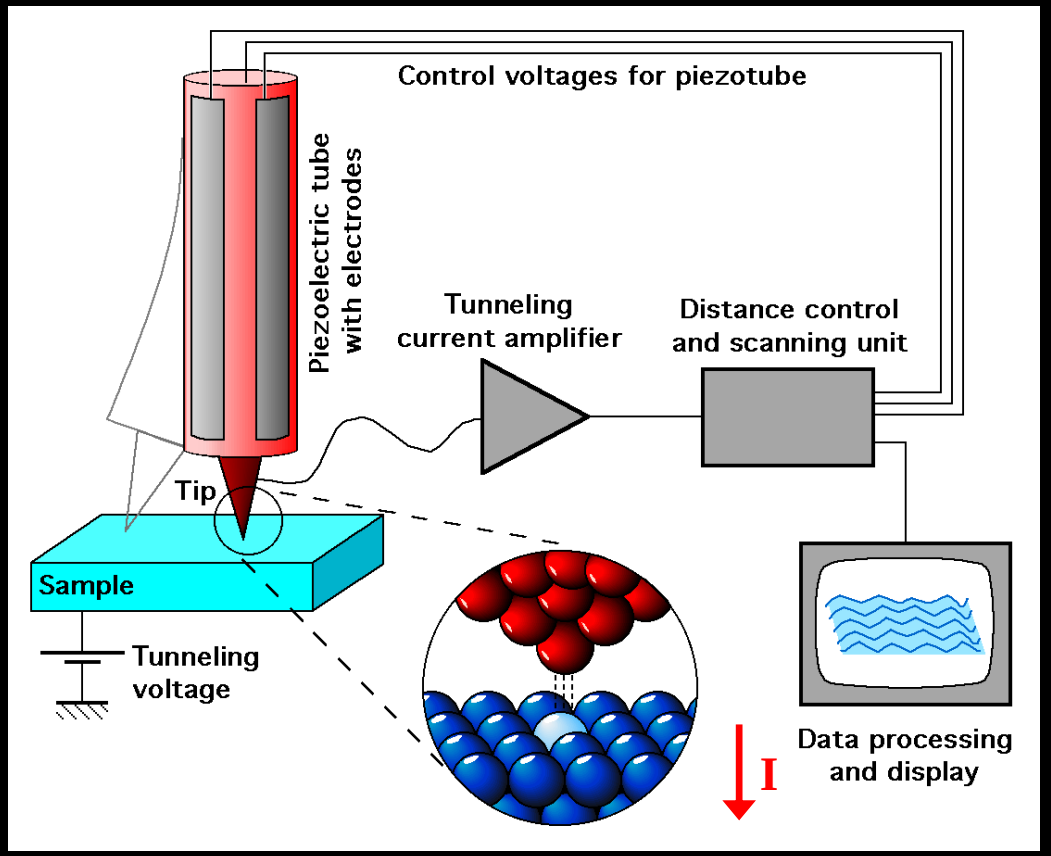

©Wikipedia

Constant Current Topography

$$I(\vec{r}, z, V) \propto \exp(-2\kappa(\vec{r})z) \int_0^{E=eV} LDOS_{sample}(\vec{r}, E)dE$$

where $\kappa(\vec{r}) = {\sqrt{2m\emptyset(\vec{r})}}/{\hbar} \sim 1\text{Å}^{-1}$

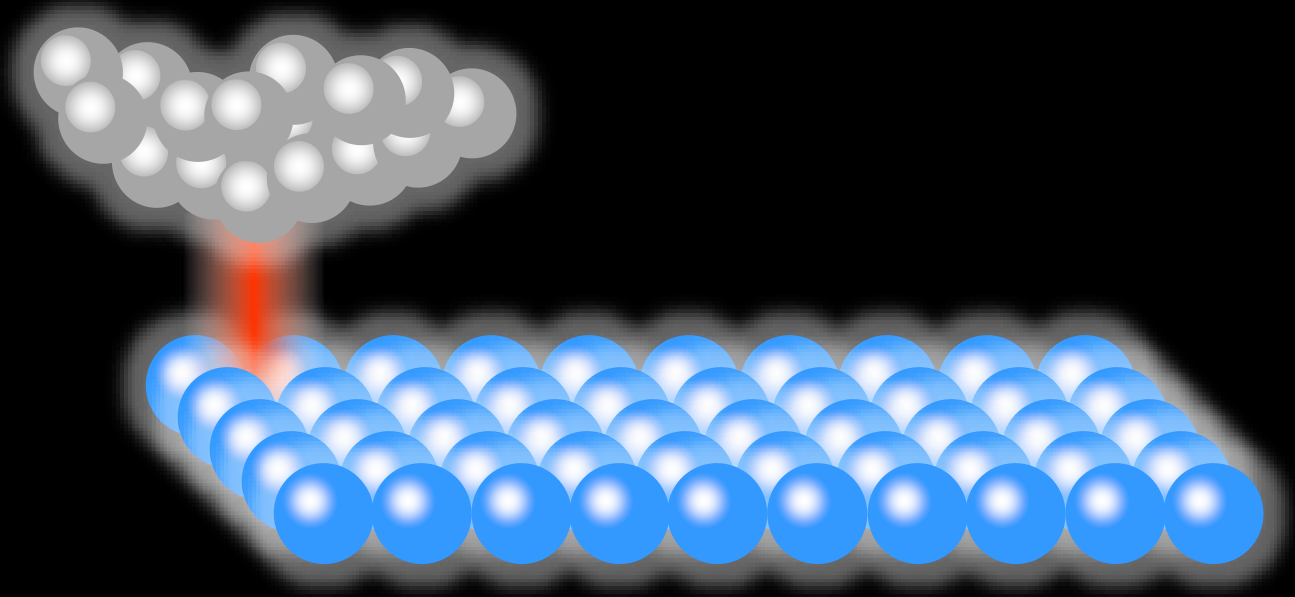

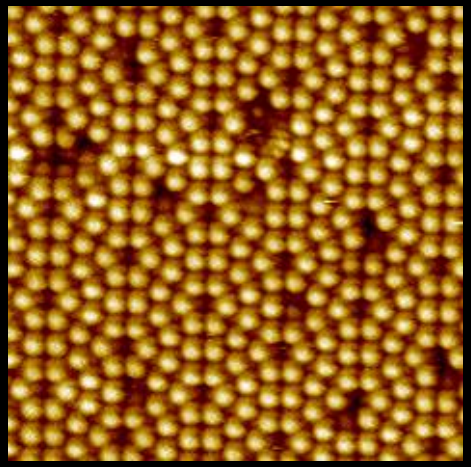

Si(111) 7x7

© Omicron Nanotechnology GmbH

Tunneling current

$$I(\vec{r}, z, V) \propto \exp(-2\kappa(\vec{r})z) \int_0^{E=eV} LDOS_{sample}(\vec{r}, E)dE$$

where $\kappa(\vec{r}) = {}^{\sqrt{2m\emptyset(\vec{r})}}/_{\hbar} \sim 1\text{Å}^{-1}$

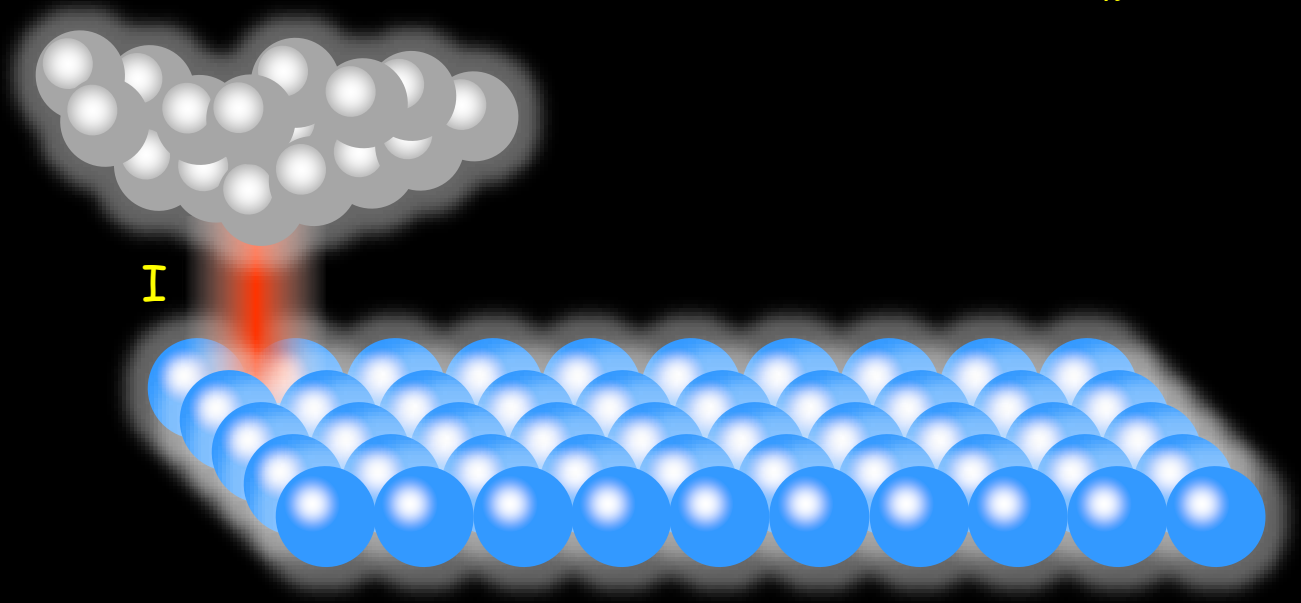

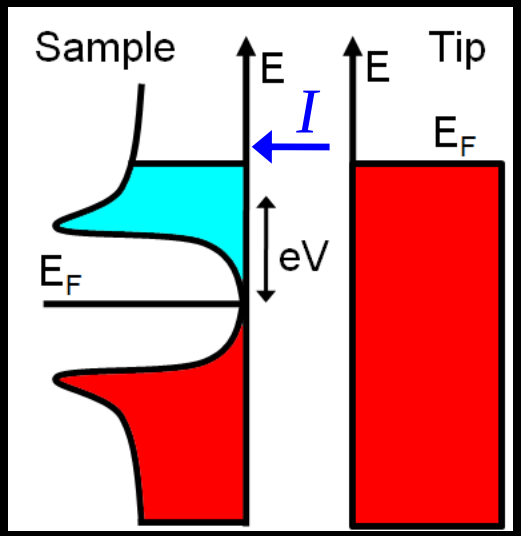

Tunneling Spectroscopy

Local Density of States : $\frac{dI}{dV}(\vec{r},V) \propto LDOS_{sample}(\vec{r},E=eV)$

$$I(V+\Delta V\sin\omega t) = I(V) + \frac{dI}{dV}\Delta V\sin\omega t + \ldots$$

Point Spectrum

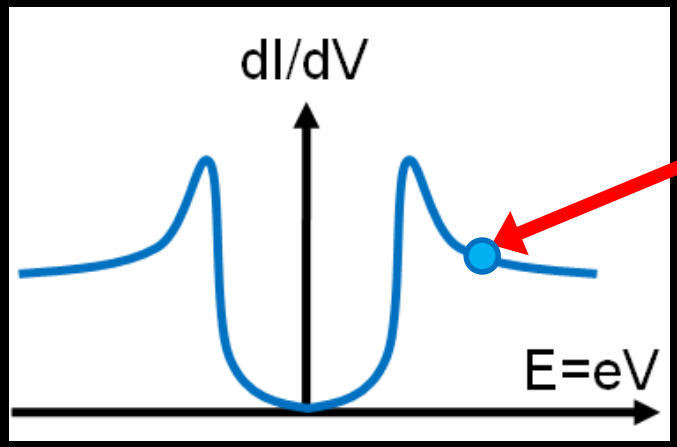

Modulation, dV

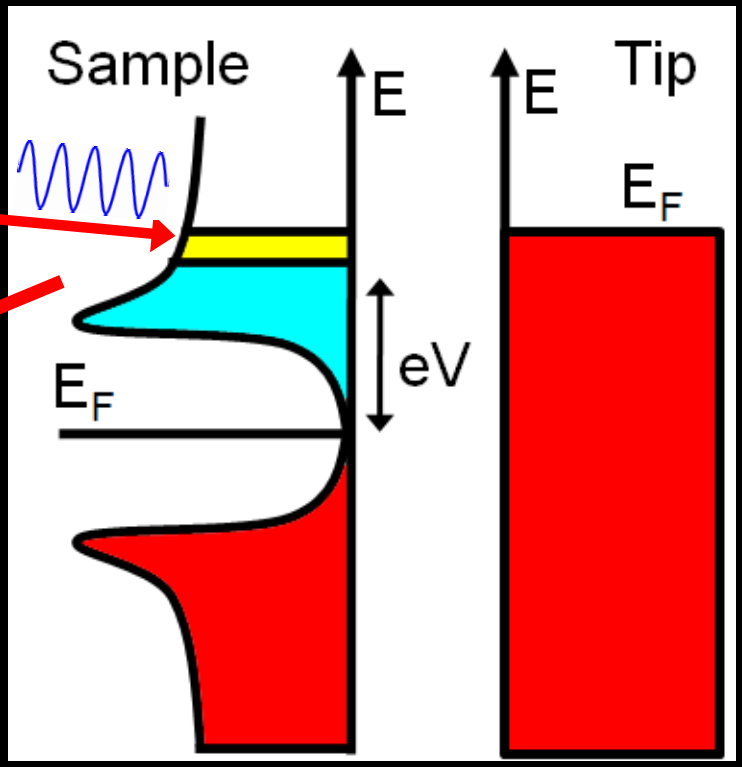

Superconducting Energy Gap by STM

Tetsuo Hanaguri

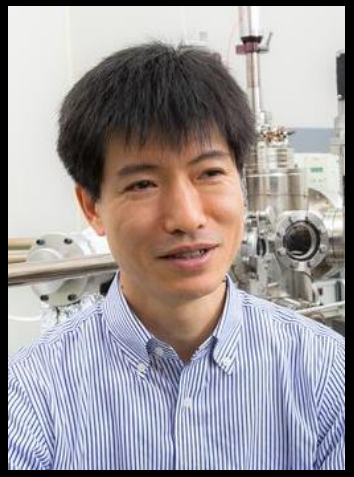

©RIKEN

Energy resolution is thermally limited.

2H-$NbSe_2$, T_c = 7.1 K, measured at $T \sim 0.4$K

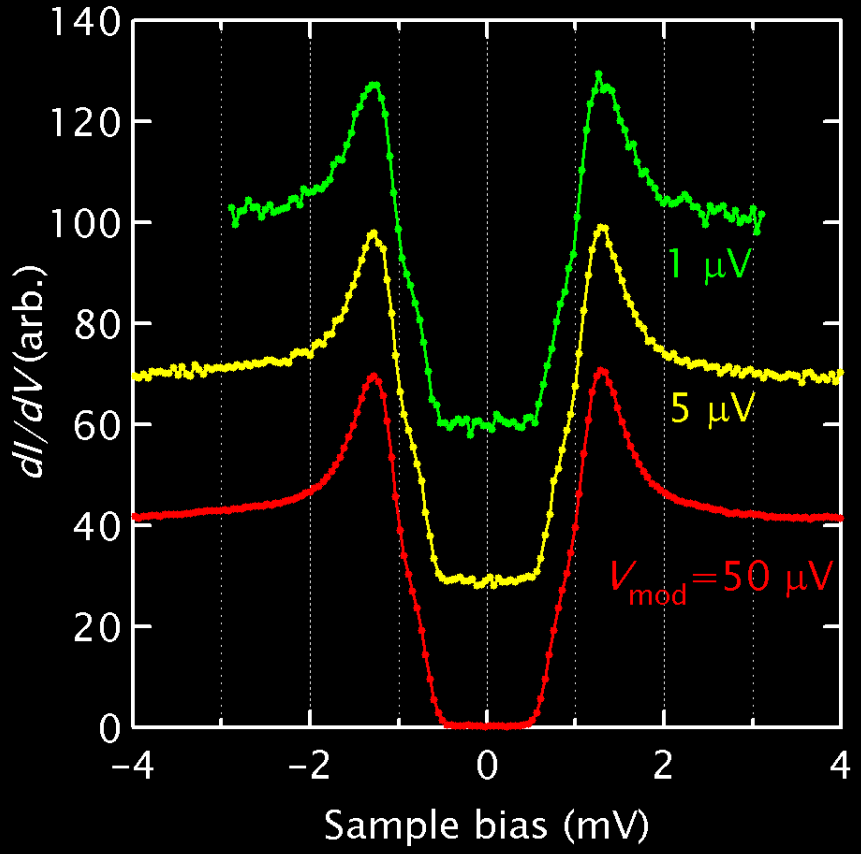

Scanning Tunneling Spectroscopy (STS) Mapping

Atomic resolution energy resolved conductance images, $g(r,E) \propto LDOS(r,E)$

Energy resolution ≤ 0.35meV at T=1.2K

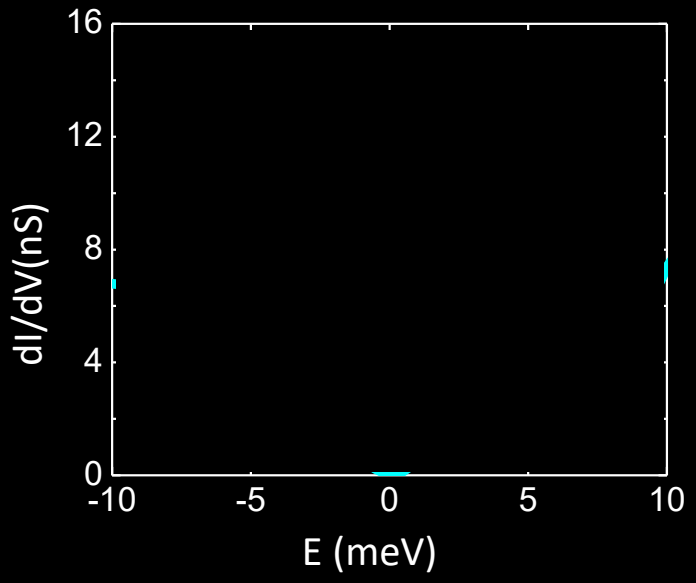

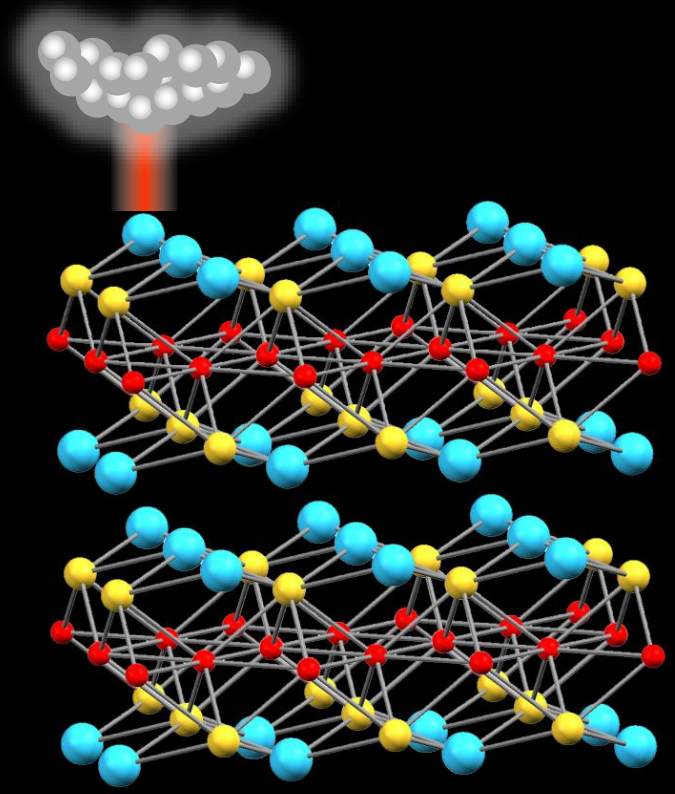

LiFeAs

Atomic Resolution Energy Resolved Images, LDOS(r,E)

~5M dI/dV(r,E):
>50ms each with S/N~100
Total measurement > 72 hours
Requires < 10^{-15} m STM-tip vibration

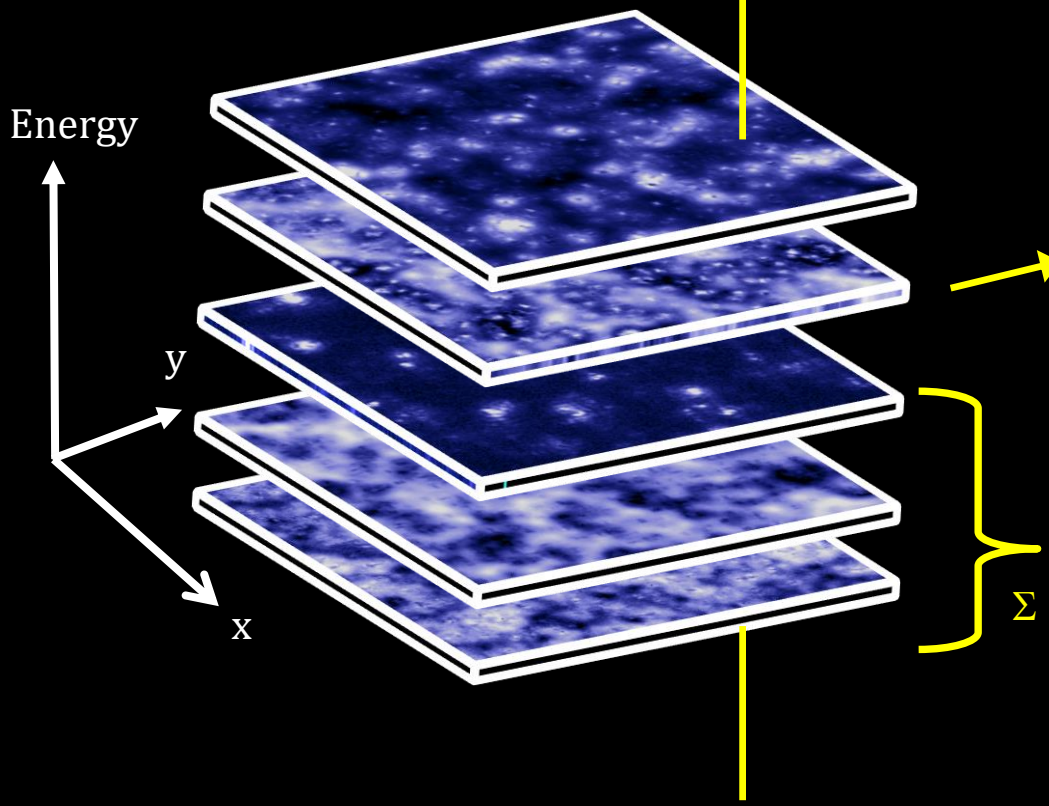

Spectrum(r)

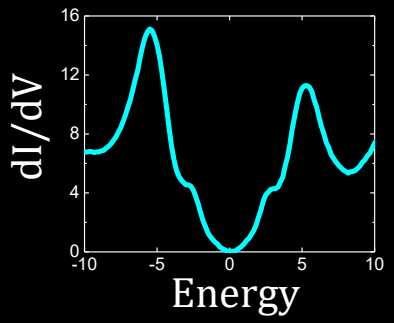

LDOS(r, E)

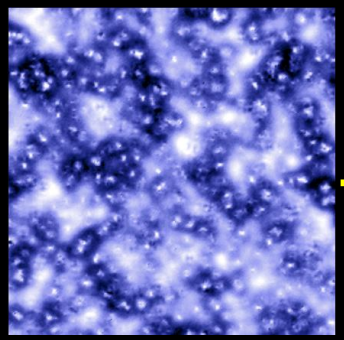

DFT

LDOS(q,E)

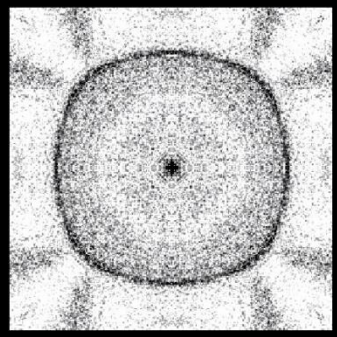

Σ

Topograph(E)

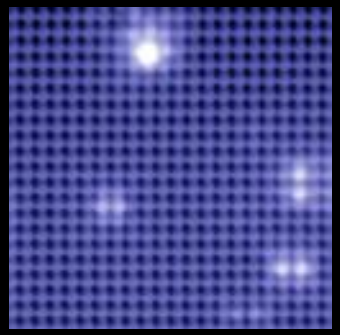

Our Resolution and Stability

STM Tip on Piezo Scanner

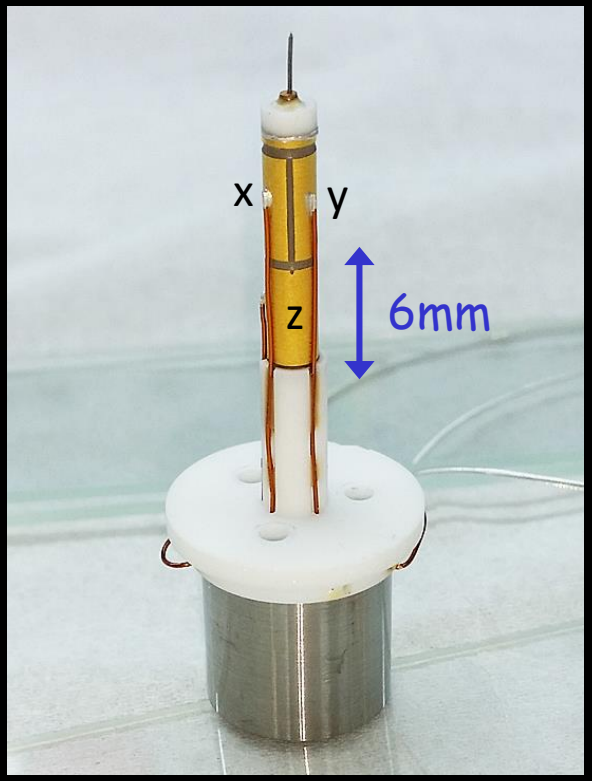

Taipei 101

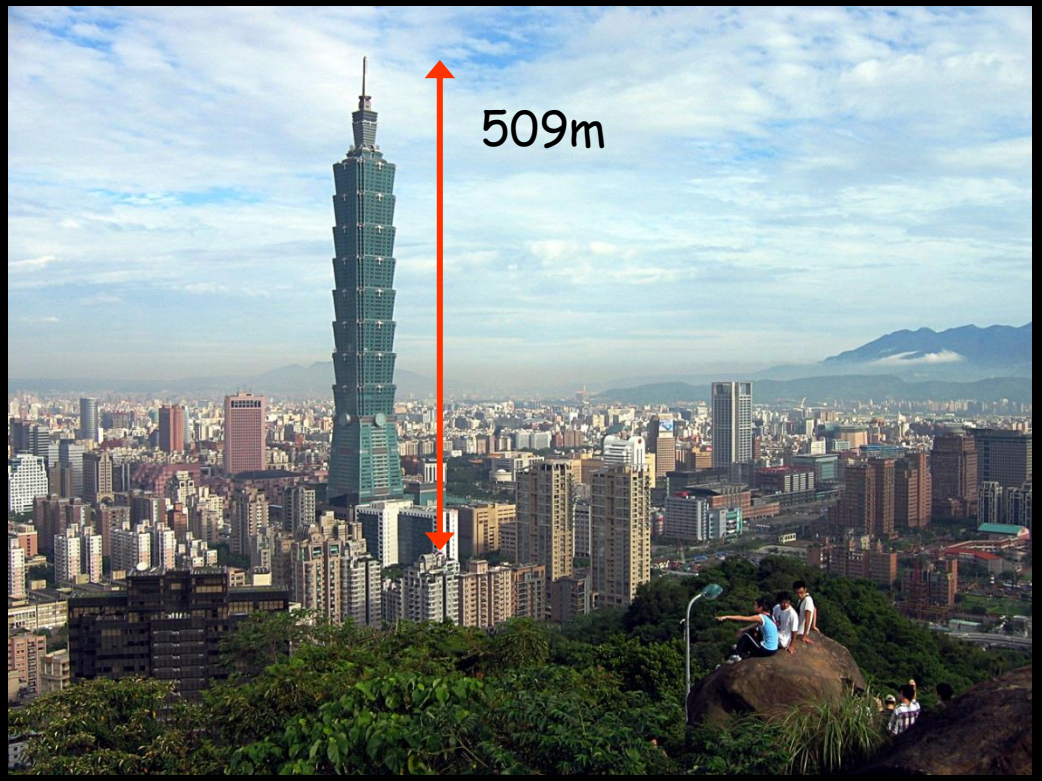

@Wikipedia

0.5pm/6mm → 42nm/509m!

Ivar Giaever

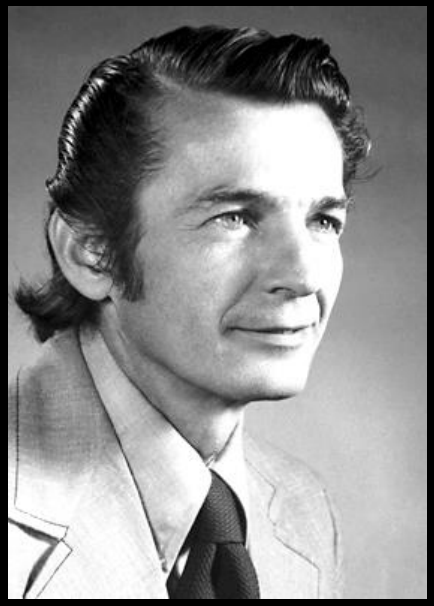

Nobel Prize 1973

The best way to do science is not to buy a big piece of expensive equipment and use it to do research. There are lots of other people who have the same big expensive equipment. The best way to do science is if you can make your own equipment, make your own thing.

- Ivar Giaever, BCS@50 Conference, 2007

愛因斯坦 (Einstein)

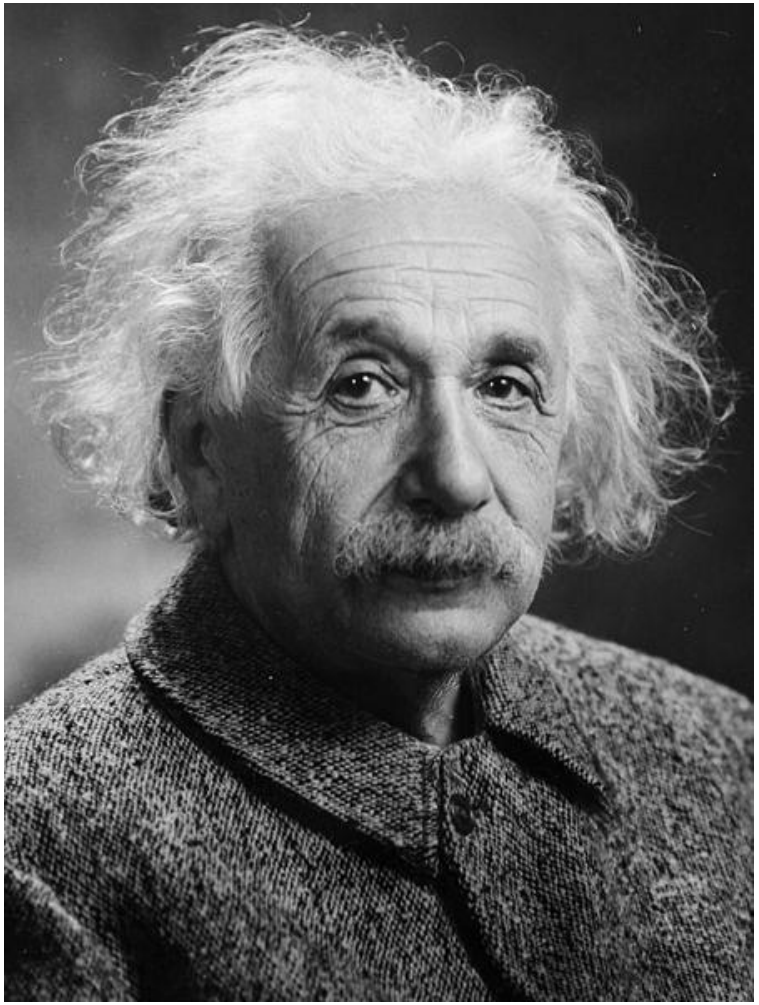

我每天提醒自己一百遍，我的生活，不管內在或是外在，都是以他人(包括活著的和逝去的)的勞動為基礎。所以我必須盡力奉獻自己，希望能以同等的貢獻，來回報長久以來(現在仍是)從他們那裡所得到的。